nature climate change

Article

https://doi.org/10.1038/s41558-025-02512-w

Resolving the changing pace of Arctic rivers

Received: 2 July 2025

Accepted: 6 November 2025

Published online: 24 December 2025

Check for updates

Emily C. Geyman & Michael P. Lamb

Arctic rivers mobilize vast stocks of permafrost carbon as they migrate across floodplains. However, there is no consensus about whether Arctic rivers are responding to regional warming by speeding up or slowing down. Here we reconstruct migration rates over the period 1972–2020 for Arctic and sub-Arctic rivers spanning approximately 1,500 km of distance and a variety of channel sizes and floodplain environments. We find that rivers in warmer, discontinuous permafrost settings experienced a systematic acceleration over the past 50 years, whereas rivers in colder, continuous permafrost regions experienced a systematic slowdown. We identify two competing mechanisms responsible for this bifurcating behaviour: thaw of permafrost floodplains has driven faster migration, whereas a decline in the intensity of river-ice breakup has slowed migration. Using a mechanistic model, we find that the relative balance of these two controls is well described by air temperature, revealing a simple organizing framework for how Arctic rivers respond to warming.

Although rivers mostly transport water and sediment downstream, they exchange a fraction of their sediment load with the floodplain by eroding sediment from their outer bank and depositing sediment on their inner bank. This interchange process is known as lateral migration because it results in the meandering or drifting of the river channel over time.

It is currently unclear whether the pace of lateral migration will increase or decrease in a warming Arctic. However, the answer affects how quickly the hundreds of gigatons of carbon currently locked up within Arctic floodplains[1,2] can be mobilized[3] and exposed to the atmosphere. Understanding whether and how river migration rates will change also is necessary for predicting the stability of Arctic infrastructure[4,5], especially in Alaska, where an estimated 43% of communities are located within 1 km of a river[6]. Despite its importance for local infrastructure and for the global cycling of carbon[7], sediment[8], nutrients[9] and pollutants[10], there is no consensus about whether Arctic rivers are responding to climate change by speeding up[11,12] or slowing down[13].

Here we seek to answer this question by looking at the recent historical record. Long-term Earth observation satellites such as those in the Landsat programme (1972–present)[14] now provide ≥50-year archives of Earth surface change. These datasets are becoming long enough to quantify changes in river migration rates over time[13]. However, measuring temporal trends from satellite data is complicated by the fact that the satellite datasets themselves have ever-improving spatial, spectral and temporal resolution[14]. Thus, robust trend detection requires measurement techniques that are unaffected by secular changes in image resolution and/or geolocation accuracy. We develop one such methodology and then use it to quantify changes in Arctic river migration rates. We combine our observations with co-located environmental datasets to test a range of hypotheses for why river migration rates are changing across space and time.

Competing processes driving faster versus slower migration

Broadly, four mechanisms have been invoked to explain a possible increase in Arctic river migration rates (Fig. 1):

(1) **Increasing water discharge**. Elevated streamflow could drive higher fluid shear stresses, causing faster riverbank erosion[15].
(2) **Increasing river temperatures**. For riverbanks that are frozen (permafrost), warmer waters could support faster rates of ablation-limited erosion[11,12,16,17].
(3) **Destabilization of riverbanks from permafrost thaw**. Floodplain permafrost degradation driven by atmospheric warming[18–20] can melt the pore ice cementing permafrost riverbanks together[16,17], causing banks to become more susceptible to erosion from the flowing river[11,16,21,22].

Division of Geological and Planetary Sciences, California Institute of Technology, Pasadena, CA, USA. e-mail: egeyman@caltech.edu

https://doi.org/10.1038/s41558-025-02512-w

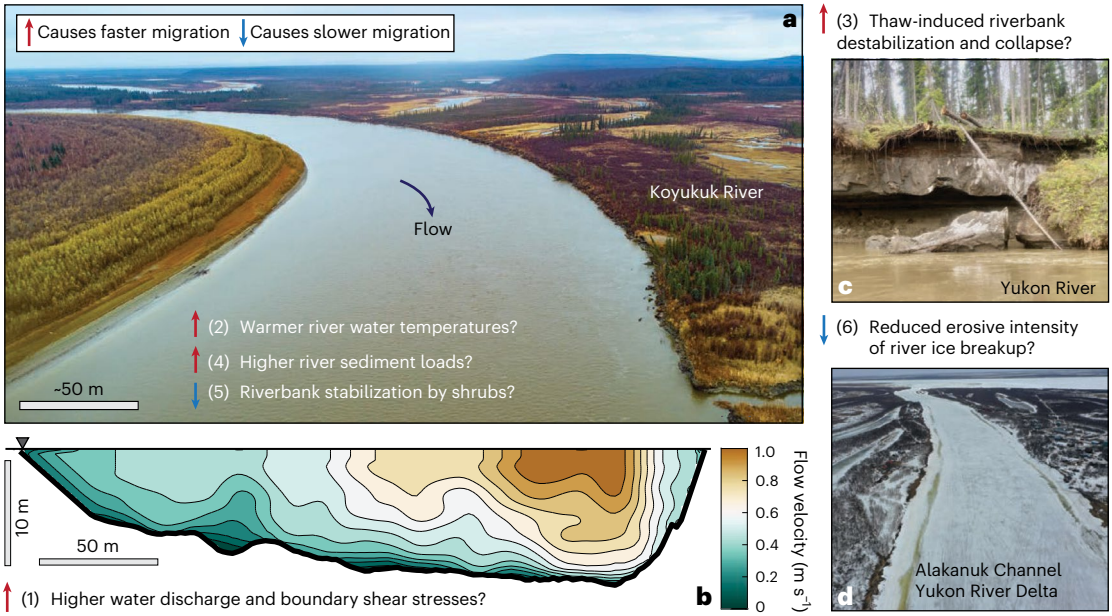

Fig. 1 | An illustration of the varied explanations for why lateral river migration may speed up (1–4) or slow down (5–6) in a warming Arctic. a, An image of the Koyukuk River near Huslia, Alaska (65.70° N, 156.38° W). **b**, A transect of river flow velocity across the Koyukuk River (**a**). The spatial gradient of the flow velocity against the riverbank records the boundary shear stress, which controls rates of sediment entrainment and erosion[16,43]. Increased water discharge in Arctic rivers[15] could drive larger shear stresses and greater bank erosion (1). In contrast, shrub growth along riverbanks could generate drag and protect sediment from the shear stresses exerted by the core of the river flow[13] (5). **c**, An example of the collapse of an ice-rich permafrost riverbank along the Yukon River near Beaver, Alaska (66.36° N, 147.40° W). **d**, An example of the ice-covered Alakanuk channel, a distributary branch of the Yukon River (62.68° N, 164.66° W), a few days before ice breakup. If springtime breakup events are a major agent of erosion[29,31], then the declining mechanical intensity of river-ice breakup[30] could reduce annual-averaged erosion rates (6). Photo in **d** from collaborator Theodore Hamilton.

(4) **Increasing riverine sediment loads**. Higher sediment loads could drive faster bar growth and faster overall migration, as has been proposed for low-latitude rivers[23]. Arctic rivers currently have anomalously low sediment concentrations[24–26], but are predicted to carry more sediment as the Arctic warms[8].

In contrast to the four processes listed above, two mechanisms could work in the opposite direction and act to decrease Arctic river migration rates (Fig. 1):

(5) **Shrub expansion**. To the extent that vegetation acts to stabilize and protect riverbanks[27], an increase in woody vegetation associated with Arctic greening[28] may act to reduce erosion[13].

(6) **A decline in the erosive intensity of river-ice breakup**. Arctic rivers are distinct from their low-latitude counterparts in part because they experience a period of river-ice breakup in the spring, during which rafts of floating ice can constrict channel flow and grind against the banks, acting as tools for erosion[29]. A decline in river-ice[30], or the intensity of river-ice breakup[29], could result in reduced rates of river migration[31].

Observational constraints from the satellite record

The opposing directionality of processes 1–6 makes it difficult to predict whether Arctic river migration rates will increase or decrease in the coming decades[32]. As Earth approaches 2 °C warming, the Arctic region is expected to reach ≥4 °C mean annual warming[33] due to the collection of sea-ice, circulation and radiation feedback broadly referred to as Arctic amplification[34]. Arctic landscapes already have warmed approximately 3 °C from the pre-industrial baseline (1850–1900)[33], a perturbation large enough to reduce permafrost coverage by a third[19,20]. In other words, Arctic landscapes are already in a state of transition[19,35], meaning that observations from the historical satellite record (past ~50 years) provide an opportunity to constrain the response of Arctic rivers to ongoing and future warming[13].

Quantifying river migration rates from satellite imagery

We analyse a large database of meandering Arctic and sub-Arctic rivers (n = 22 distinct river reaches) spanning 1,486 km in distance (Fig. 2a). We focus the majority of the sites in Alaska because this region has an observationally constrained map of permafrost abundance[36].

Note that any analysis seeking to discern change over time from satellite data must contend with the non-stationarity in the spatial resolution, spectral resolution and geolocation accuracy of satellite datasets[14]. For example, the nine satellites of the Landsat programme (1972 to the present) have acquired imagery with steadily improving spatial resolution from 80 m per pixel to 15 m per pixel[14]. Since image georeferencing errors, which are typically on the scale of half a pixel[37], are erroneously measured as channel migration using the existing centreline[13,38,39] and/or area-based[40] techniques (Extended Data Figs. 1 and 2), this steadily improving satellite spatial resolution may lead to a bias that indicates a widespread slowdown in Arctic river migration rates, even if no such slowdown exists.

Using a series of numerical experiments (see Methods), we find that this bias is significant and sufficient to explain the magnitude of a recently reported slowdown in Arctic river migration rates[13] (Extended Data Figs. 1–3). Thus, we devise a different methodology for quantifying river migration that is unbiased with respect to changing georeferencing accuracy.

Briefly, our approach leverages the fact that the first-order control on the migration rates of meandering rivers is the channel curvature[38]. Comparing a river's dimensionless curvature (channel width [m] divided by radius of curvature [m]) to its local migration rate (m yr^{-1}) reveals a quasi-linear relationship[38] with a slope k (m yr^{-1}), deemed the 'erodibility coefficient' (Fig. 2b). For any pair of images, k can be

https://doi.org/10.1038/s41558-025-02512-w

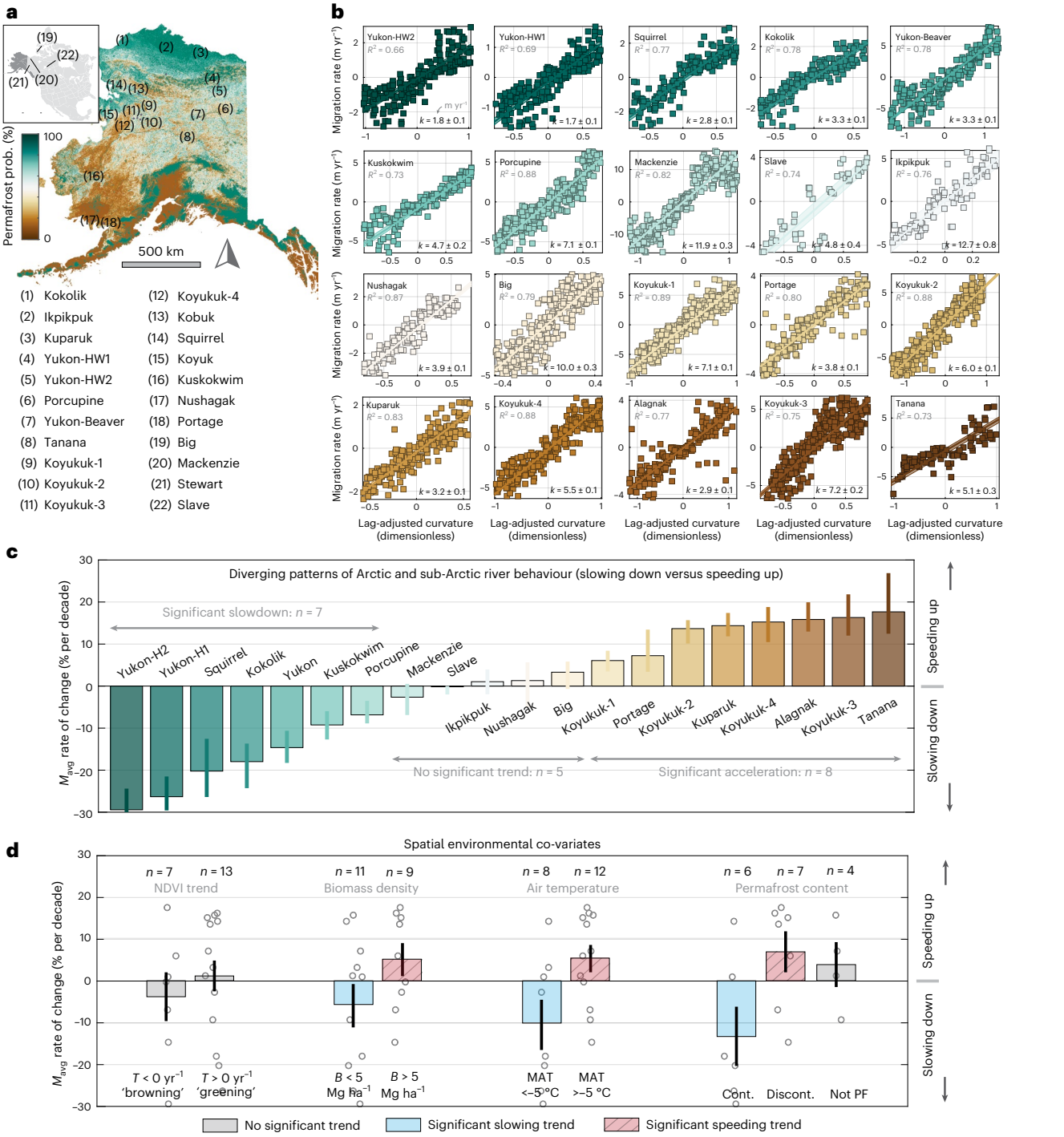

Fig. 2 | Estimated changes to Arctic river migration rates during the Landsat satellite record. a, Locations of the river reaches analysed in this study, including the $n = 10$ Arctic river reaches from ref. 13, plus an additional $n = 12$ reaches added in this study to increase the sampling of different permafrost terrains. **b**, Relationships between lag-adjusted curvature and local migration rate for the investigated reaches. The error envelopes in **b** represent the $\pm 1\sigma$ uncertainty ranges of the linear fits. In total, 20 of the 22 rivers shown in **a** support the first-order control of river curvature on migration rate[38]. The Kobuk and Stewart rivers were found to have poor regression relationships, and were therefore excluded from subsequent analysis (see Supporting Information for a discussion). **c**, Results of the temporal trend analysis. M_{avg} denotes the reach-averaged migration rate (equation (12)), and the error bars depict the 25th–75th percentile uncertainty range of the estimated M_{avg} trend, as illustrated in Supplementary Figs. 5–8. **d**, Exploration of four environmental co-variates for the opposing slowdown versus acceleration behaviour in **c**, including the greening versus browning NDVI trend[41], average floodplain aboveground biomass density[42], and the mean annual air temperature and permafrost content, based on the map of ref. 36. The $n = 3$ rivers located in Canada are not included in the permafrost content analysis because they lie outside the domain of the permafrost map[36]. Floodplains are classified as continuous permafrost (cont.), discontinuous permafrost (discont.) or not permafrost (not PF) on the basis of their average permafrost probability: 70–100%, 30–70% or 0–30%, respectively. In **c**, error bars represent the 25th–75th percentile range of the temporal trend estimates derived from the bootstrap resampling described in Methods. Bar heights denote the 50th percentile. In **d**, error bars represent ±1 s.e. ($\sigma/\sqrt{n}$) for the n river reaches that fall within each category. Bar heights denote the mean value within each category. MAT, mean annual temperature.

estimated by regressing the local migration rate to the lag-adjusted curvature[38] (Fig. 2b). Then, the reach-averaged migration rate (M_{avg}) can be calculated by averaging the product of the erodibility coefficient and the dimensionless curvature (equation (12)). The advantage of calculating river migration rates using this curvature-based approach is that it avoids the overcounting of apparent channel migration that results from image-to-image geolocation errors (Extended Data Fig. 1). Using numerical simulations, we find that this curvature-based approach is nearly an order of magnitude less sensitive to secular changes in image resolution and co-registration errors over the Landsat satellite record than the existing approaches[13,38–40] (Extended Data Fig. 3e,f). Of the total $n = 22$ meandering reaches investigated in this study, $n = 20$ produce robust relationships between the lag-adjusted curvature and local migration rate (Fig. 2b). These are the reaches we analyse for temporal trends in migration rate. For a complete description of the data processing, trend analysis and significance testing, see Methods.

Arctic rivers exhibit diverging speeding versus slowing trends

We find that, of the $n = 20$ investigated river reaches with robust curvature-dependent migration rates (Fig. 2), $n = 7$ (35%) exhibit a statistically significant slowdown over the Landsat observational record, $n = 8$ (40%) exhibit a statistically significant acceleration, and $n = 5$ (25%) show no detectable trend. In other words, approximately equal proportions of the investigated rivers have sped up as have slowed down (Fig. 2).

Physical and environmental controls on migration

We explore whether there are physical or environmental variables that are significant predictors of whether river migration has sped up or slowed down over the past five decades. First, we leverage environmental variability across space to identify the physical controls on migration behaviour. We divide the dataset of investigated rivers into discrete categories on the basis of their: (1) floodplain greening versus browning trend[28,41], (2) floodplain vegetation (quantified using the regional aboveground biomass density[42]), (3) mean annual temperature and (4) floodplain permafrost classification (continuous permafrost, discontinuous permafrost or no permafrost)[36] (Fig. 2d).

We do not observe a statistically significant difference in the migration behaviour of rivers traversing landscapes that are greening versus browning[41], a result that challenges the shrubification hypothesis for changing Arctic river migration rates[13]. However, we observe significant relationships between the migration trends (acceleration versus deceleration) and (1) biomass density, (2) mean annual temperature and (3) permafrost content (Fig. 2d). Rivers with floodplains that have high biomass densities[42] (that is, those that are forested) tend to be speeding up, while rivers with low biomass densities tend to be slowing down. Likewise, rivers traversing the coldest landscapes are slowing down whereas rivers traversing warmer terrains (with mean annual temperatures approaching 0 °C) are speeding up. Finally, rivers in continuous permafrost experienced a significant slowdown (−13.0 ± 7.0% per decade). Rivers in discontinuous permafrost experienced a significant acceleration (6.8 ± 4.8% per decade). Rivers in regions classified as having no permafrost experienced no statistically significant trend in migration rates.

Temporal trend analysis

We build on the analysis of spatial environmental co-variates in Fig. 2d and use temporal trends to explore what processes could explain the bifurcating migration behaviour. As introduced in Fig. 1, six possible explanations for changing river migration rates include: (1) changes in water discharge, (2) changes in river temperatures, (3) permafrost thaw on floodplains, (4) changes in riverine sediment loads, (5) shrubification of riverbanks and (6) changes in the erosive intensity of river-ice breakup.

Although all of the items listed above have been posed in the literature, few have been compared to co-located observations of migration rates. We hypothesize that, to explain the bifurcating observations in Fig. 2c, there must be one or more processes driving the acceleration in migration rates and one or more processes driving the slowdown. Further, we posit that the relative influence of these competing processes determines where a particular river lies along the speeding versus slowing spectrum. We make pairwise comparisons to test whether the observed migration rate trends (Fig. 2c) could be explained by processes 1–6.

Figure 3g–l shows this suite of pairwise comparisons, where each data point represents a river from Fig. 2. We find no statistically significant relationship between a river's migration rate trend and its (1) changes in water discharge, (2) changes in water temperature, (4) changes in sediment load or (5) floodplain greening versus browning. However, we find that two of the proposed mechanisms: (4) permafrost thaw on floodplains and (6) declining intensities of river-ice breakup, produce statistically significant relationships that could be responsible for the diverging increase versus decrease in riverbank erosion rates (Fig. 2c). As a final analysis, we use a mechanistic model[11,16] to test whether these two processes are sufficient to explain the magnitude and directionality of the observed historical trends.

Leveraging a mechanistic model for riverbank erosion

In the conceptual framework of our Arctic riverbank erosion model, for a river to erode a permafrost bank, the river must both: (1) conduct sufficient heat into the bank to thaw the pore ice cementing sedimentary particles and (2) have sufficient water flow (boundary shear stress) to transport the thawed sediment[16] (Fig. 4). Immediately following spring-time ice breakup, the river flow is strong, but the water temperature is near 0 °C, so erosion is limited by the river's ability to thaw the bank (that is, 'thaw-limited'). In contrast, in mid-summer, the warm river water can rapidly thaw the bank, but the flow is too weak to transport the thawed sediment (that is, 'entrainment-limited'). The total erosion is described by the minimum of the thaw-limited and entrainment-limited curves[16]. Changing patterns of water discharge (for example, an increase in the frequency of summer rainstorms) (Fig. 4b) and changing patterns of water temperature (for example, an increase in summer water temperatures) (Fig. 4c) can cause the total erosion to increase. Alternatively, if the floodplain undergoes widespread permafrost thaw due to atmospheric warming[18], riverbank erosion becomes constrained only by the entrainment-limited model, and the total annual erosion can increase[11] (Fig. 4d). The model in Fig. 4 was previously tested and validated using high-resolution observations from the Koyukuk River (Fig. 1a), where it successfully reproduced the spatial and temporal patterns of riverbank erosion[11].

Model description and governing equations

We express the total riverbank erosion rate (E_{total}, $[L\ T^{-1}]$), which is equal to the reach-averaged migration rate (M_{avg}) for channels that maintain constant width over time (a good approximation for our investigated reaches; see Methods), as:

$$E_{total} = \text{argmin}\{E_{ent}, E_{thaw}\} + E_{ice} \quad (1)$$

where E_{ent}, E_{thaw} and E_{ice} are the erosion contributions from entrainment-limited, thaw-limited and ice-limited erosion, respectively (Fig. 4a). For low-latitude rivers unaffected by river ice or frozen riverbanks, the total erosion rate is thought to be well described by the entrainment term (E_{ent})[16,43,44]. We represent entrainment-limited erosion using the common threshold formulation[44], adapted to mixtures of sediment and ice[16]:

$$E_{ent} = \frac{B}{\rho_b f_{sed}}\left(\frac{\tau}{\tau_c} - 1\right)^n \quad (2)$$

https://doi.org/10.1038/s41558-025-02512-w

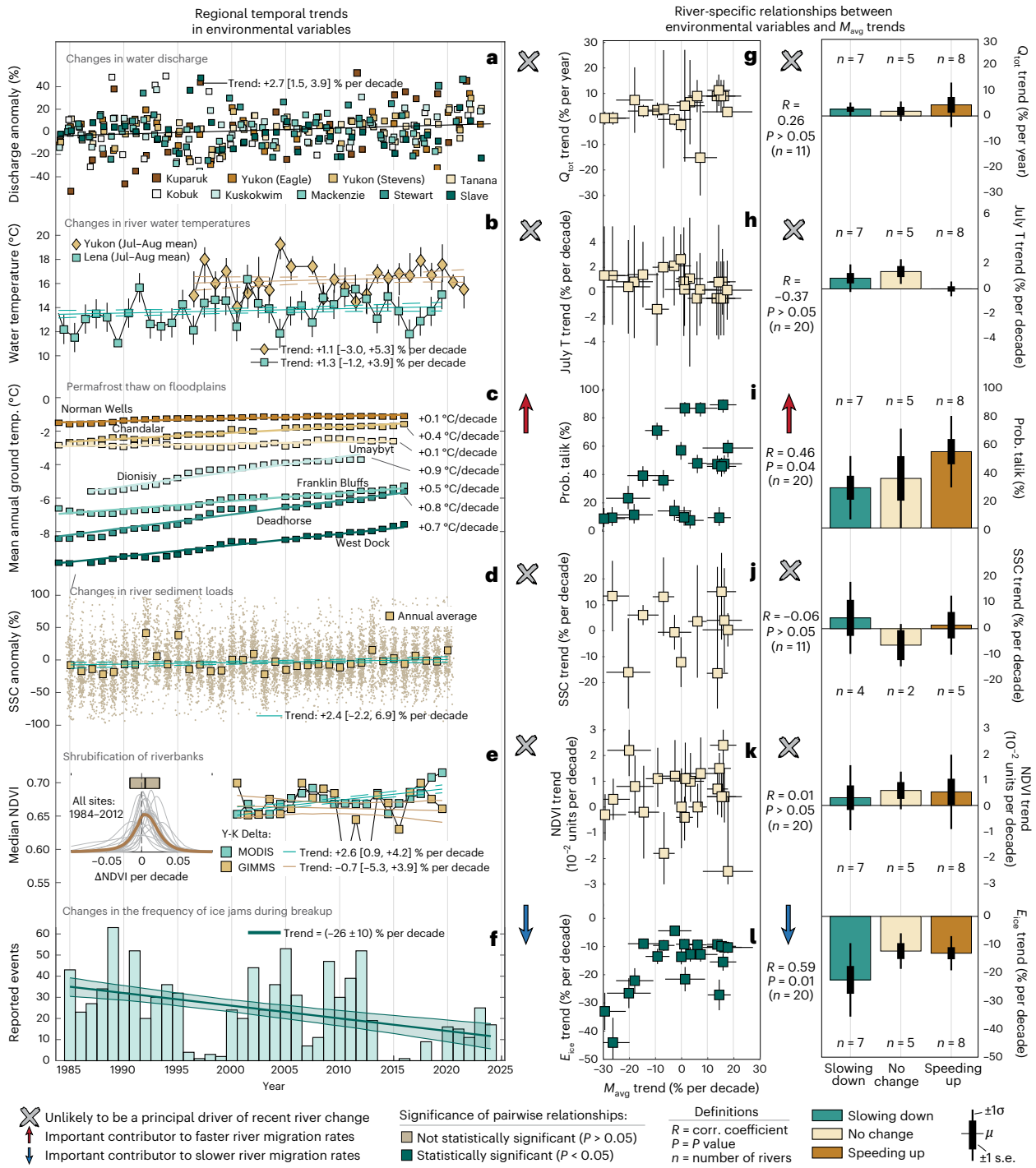

Fig. 3 | Analysis of the six possible drivers of changing Arctic river migration rates posed in Fig. 1. The left column (**a**–**f**) shows representative timeseries. The middle column (**g**–**l**) shows pairwise comparisons between each river's migration rate (M_{avg}) trend and the trend in the environmental parameter of interest. The right column clusters the same data from **g**–**l** into three groups for rivers that are slowing down, speeding up or experiencing no significant change in migration rates. In the timeseries in **a**–**f**, the values printed in brackets denote the 95% confidence intervals of the fitted linear trends. The plotted datasets in **a**–**f** include: water discharge from streamgauge records (**a**), summertime river water temperature (Yukon and Lena rivers) (error bars depict the interquartile range of water temperatures) (**b**), mean annual ground temperatures at monitoring stations across the Arctic[51] (**c**), suspended sediment concentrations (SSCs) of Arctic and sub-Arctic rivers in Alaska and Canada, based on the dataset of ref. 26 (**d**), floodplain greening versus browning trends for the Yukon-Kuskokwim (Y-K) Delta[55], with an inset histogram showing the long-term (1984–2012) floodplain greening versus browning trends for all investigated river reaches[41] (**e**), and estimates of the frequency of ice jam events in Alaska during springtime river-ice breakup, based on the database maintained by the Cold Regions Research and Engineering Laboratory (CRREL)[47] (**f**). The data in **a**–**f** are plotted from 1985 to the present (rather than 1972–present) because several of the datasets only extend to 1985[26,41]. In the crossplots in **g**–**l**, each data point represents one of the rivers in Fig. 2. The error bars in **g**–**h** and **j**–**l** depict the ±1σ uncertainties of the calculated linear temporal trend for each river. Error bars for the y axis in **i** depict the estimated uncertainty of the talik probability, which is calculated using the lower and upper bounds of the sigmoidal relationship shown in Supplementary Fig. 28. Significance of the pairwise relationships in **g**–**l** was assessed using the two-sided Pearson correlation coefficient $R(x, y)$ and the associated P value (not adjusted for multiple comparisons). See Methods for details of each dataset. Only two drivers: (3) permafrost thaw on floodplains and (6) changes in the frequency of river-ice jams, reveal significant relationships with the observed migration rate trends.

https://doi.org/10.1038/s41558-025-02512-w

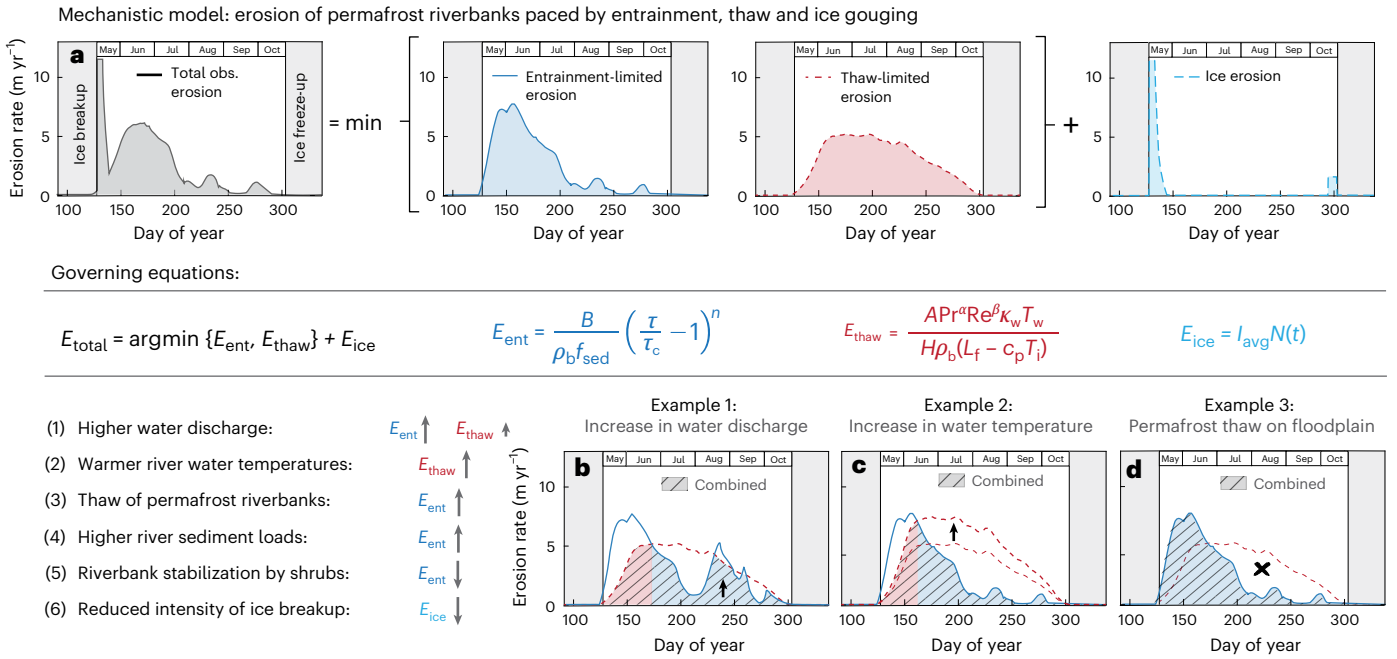

Fig. 4 | A simple mechanistic model for riverbank erosion in permafrost landscapes. a, Illustration of the seasonal timeseries of erosion rates from ice breakup in May to ice freeze-up in October, after ref. 16. The erosion of permafrost riverbanks is controlled by the dual constraint of thawing the pore ice cementing bank sediment (thaw-limited erosion) and transporting the thawed sediment (entrainment-limited erosion)[16]. **b**–**d**, Based on the theoretical framework in **a**, there are three ways to increase erosion rates along permafrost rivers: increasing the water discharge (especially water discharge in the mid-summer, when erosion tends to be entrainment limited[11,16]) (**b**), increasing the water temperature (**c**) and thawing the floodplain (**d**), such that the eroding riverbank is no longer subject to the thaw-limited model.

where τ (Pa) is the fluid shear stress exerted on the riverbank, τ_c (Pa) is the critical shear stress required to entrain bank sediment, $f_{sed} = 1 - f_{ice}$ (kg kg^{-1}) is the mass fraction of sediment in the bank material (f_{ice} [kg kg^{-1}] is the mass fraction of water ice), B (kg m^{-2} s^{-1}) is an empirical coefficient describing the erodibility of bank material[44], and n (dimensionless) is an exponent capturing the scaling behaviour between the excess shear stress and the erosion.

The rate of thaw-limited erosion (E_{thaw}) has been constrained from laboratory, field-based and theoretical investigations[11,16,45,46], and can be expressed in terms of the river hydraulics, river temperature and bank material properties[16]:

$$E_{thaw} = \frac{A}{\text{Pr}^\alpha \text{Re}^\beta \kappa_w T_w} H\rho_b(L_f - c_p T_i) \quad (3)$$

where A, α and β are dimensionless empirical coefficients[16,45,46], $\text{Pr} = \nu/\chi$ is the Prandtl number, ν (m^2 s^{-1}) is the kinematic viscosity of water, χ (m^2 s^{-1}) is the thermal diffusivity of water, $\text{Re} = HU/\nu$ is the Reynolds number, U (m s^{-1}) is the mean flow velocity, κ_w (W m^{-1} °C^{-1}) is the thermal conductivity of water, T_w is the river water temperature (°C), T_i is the initial temperature of the permafrost riverbank (°C), H (m) is the river flow depth, ρ_b (kg m^{-3}) is the bulk density of the permafrost riverbank, L_f (J kg^{-1}) is the permafrost latent heat of fusion (calculated as $L_f = f_{ice}L_{ice}$, where L_{ice} (J kg^{-1}) is the latent heat of fusion for water ice), and c_p (J kg^{-1} °C^{-1}) is the permafrost heat capacity. Note that we define E_{thaw} only for $T_w \geq 0$.

Finally, the erosion caused by river-ice breakup is parameterized as a function of the number of high intensity river-ice breakup events ($N(t)$):

$$E_{ice} = I_{avg}N(t) \quad (4)$$

where we constrain $N(t)$ using a database of ice jams from the CRREL[47] (Fig. 3f). I_{avg} (m yr^{-1}) is a parameter describing the average erosion caused by ice during breakup[31].

Constructing erosion budgets for well-constrained rivers

We use the modelling framework above to construct an erosion budget for two river reaches: the Yukon River near Beaver, Alaska (site 7 in Fig. 2a) and the Koyukuk River near Huslia, Alaska (site 9 in Fig. 2a). We choose these two reaches because they are the only two sites for which we have in situ field measurements of flow hydraulics, sediment transport, sediment grain size, bank material properties, water temperature and water discharge[11,48], allowing us to validate the model parameters for equations (1)–(4).

Moreover, these two sites present useful case studies because they have similar average migration rates (2.8 m yr^{-1} versus 2.7 m yr^{-1}), but the two sites differ in climatic regime and their speeding versus slowing trends (Fig. 2). The site on the Yukon River has a colder mean annual temperature, colder and more stable permafrost[49], and has experienced a systematic slowdown in migration over the past 50 years ($\Delta M_{avg} = -14.6 \pm 5.9\%$ per decade). In contrast, the site on the Koyukuk River has a warmer mean annual temperature, warmer and patchier permafrost[49], and has experienced a systematic increase in migration rates over the past 50 years ($\Delta M_{avg} = +6.1 \pm 3.5\%$ per decade) (Extended Data Tables 1 and 2).

Streamflow, water temperature and air temperature datasets (see Methods) jointly constrain the permafrost erosion model in Fig. 4 and allow us to hindcast the annual signal of entrainment-limited and thaw-limited erosion at both sites. Since both sites in Fig. 5 are located in discontinous permafrost landscapes, we must account for the fact that the meandering Yukon and Koyukuk rivers encounter a mix of riverbanks that are permafrost versus not permafrost. On the permafrost riverbanks, we apply the dual thaw- and entrainment-limited model (Fig. 4b,c). On the non-permafrost riverbanks, we apply the entrainment-only model (Fig. 4d). Next, we allow regional permafrost thaw and talik formation[18] to change the fraction of permafrost coverage in the floodplain landscape as a function of time (ranging from 0% to −1% per year change in floodplain permafrost abundance[20,50]; see Methods). That is, we allow permafrost degradation forced by

https://doi.org/10.1038/s41558-025-02512-w

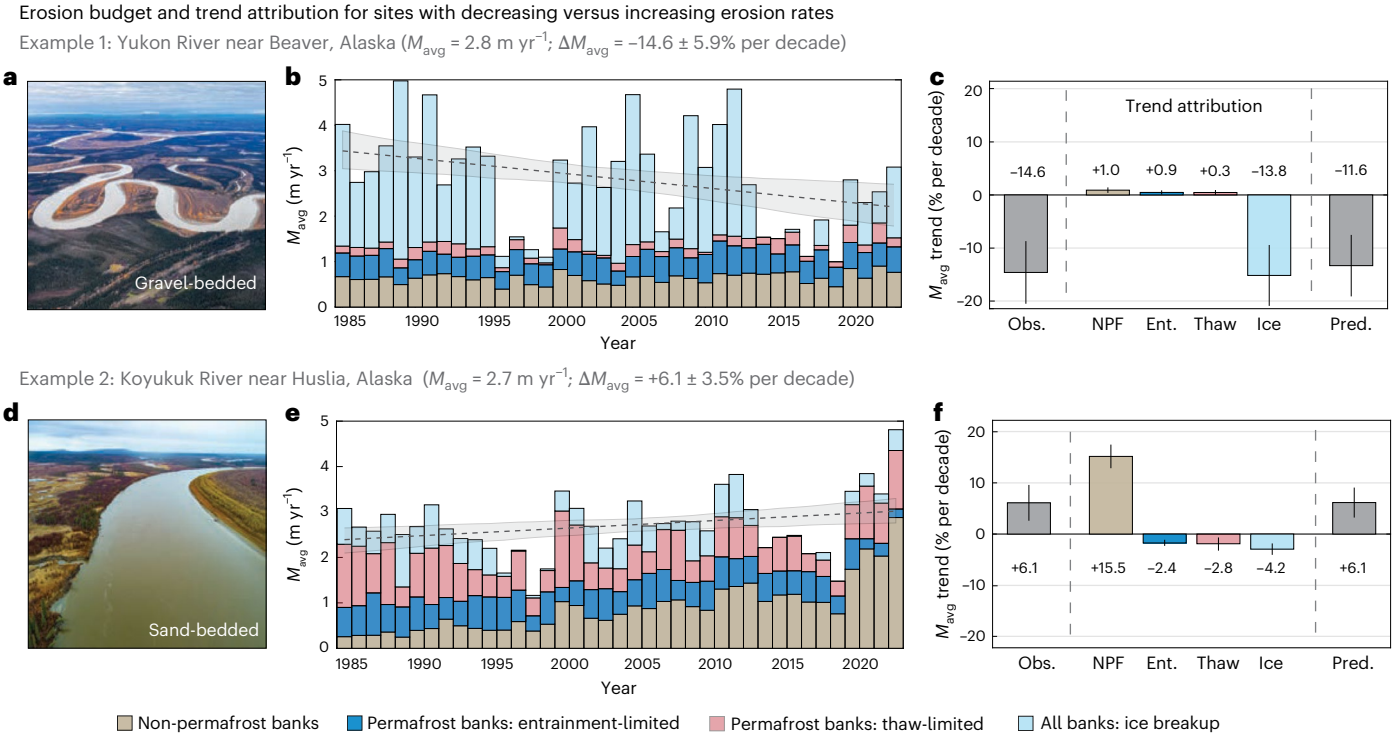

Fig. 5 | Trend attribution for rivers with decreasing versus increasing reach-averaged migration rates (M_{avg}). **a**–**f**, We apply the model in Fig. 4 to construct an annual erosion budget for the period 1985–2025 (same timeframe as the data in Fig. 3) for two different river reaches: the Yukon River near Beaver, Alaska (66.362° N, 147.398° W; site 7 in Fig. 2a) (**a**–**c**) and the Koyukuk River near Huslia, Alaska (65.700° N, 156.387° W; site 9 in Fig. 2a) (**d**–**f**). Panels **b** and **e** show the annual timeseries of migration rates attributed to erosion of non-permafrost banks (entrainment-limited), permafrost banks (entrainment- and thaw-limited) and erosion during ice breakup. The dashed lines represent the linear fits through the timeseries. Panels **c** and **f** show the trend attribution of the decreasing (**c**) or increasing (**f**) migration rates over time. In **c**, the observed M_{avg} trend is −14.6 ± 5.9% per decade and the modelled M_{avg} trend is −11.6 ± 5.5% per decade. In **f**, the observed M_{avg} trend is +6.1 ± 3.5% per decade and the modelled M_{avg} trend is +6.1 ± 3.6% per decade. The error bars in **c** and **f** represent the ±1σ uncertainties calculated from the temporal trends shown in **b** and **e**, respectively. Obs., observed erosion; NPF, predicted erosion of non-permafrost banks; Ent., predicted entrainment-limited erosion of permafrost banks; Thaw, predicted thaw-limited erosion of permafrost banks; Ice, predicted ice-breakup erosion of all banks; Pred., total predicted erosion.

atmospheric warming to change the fraction of the floodplain that is permafrost versus not permafrost[18].

To summarize, the two tunable parameters introduced in our modelling framework include: (1) the rate of floodplain permafrost thaw (R_{thaw}; [% yr^{-1}]) and (2) the average erosion caused by ice breakup (I_{avg}; [m yr^{-1}]). We perform a simple inversion to test whether there are combinations of floodplain thaw rates and average ice erosion rates that allow successful reconstruction of both the time-averaged erosion rates and the speeding versus slowing trends.

Results of the mechanistic riverbank erosion model

The Yukon River observations are well explained by the model in which average erosion due to ice breakup is ~1.5 m yr^{-1} and the floodplain has undergone permafrost thaw at a rate of 0% yr^{-1} (Fig. 5a–c). This model successfully reproduces the time-averaged erosion rate of 2.8 m yr^{-1} and predicts an M_{avg} trend of −11.6 ± 5.5% per decade, which is within error of the observed M_{avg} trend of −14.6 ± 5.9% per decade. Likewise, the Koyukuk River observations are well explained by a model in which the average erosion caused by ice gouging is ~0.4 m yr^{-1} and the floodplain has undergone permafrost thaw at a rate of 1% yr^{-1} (Fig. 5d–f). This model successfully reproduces the time-averaged erosion rate of 2.7 m yr^{-1} and produces a predicted M_{avg} trend of +6.1 ± 3.6% per decade, which is within error of the observed M_{avg} trend of +6.1 ± 3.5% per decade. See Methods for additional details.

The exercise in Fig. 5 shows that both the direction and magnitude of the bifurcating decreasing versus increasing migration rates (Fig. 2c) are readily explained by changing ice breakup intensities and floodplain permafrost thaw. The inferred ice erosion rates (0.4–1.5 m yr^{-1}) and floodplain permafrost thaw rates (0–1% yr^{-1}) agree with independent constraints of ice erosion[31] and permafrost thaw[18,20].

A conceptual model for the diverging migration rate trends

Our results suggest that Arctic and sub-Arctic rivers are experiencing two simultaneous perturbations. First, atmospheric warming is driving floodplain permafrost thaw and talik formation[18], which accelerates migration rates[11] because the mechanism of riverbank erosion transitions from being limited by the dual constraint of thaw and entrainment (Fig. 4b,c) to the singular constraint of entrainment[11] (Fig. 4d). Importantly, Arctic landscapes have undergone variable amounts of permafrost thaw in the past several decades[18]. For example, the coldest environments have experienced significant ground temperature warming[51], but temperatures are still cold enough for permafrost to remain stable (Fig. 3c). The sites in warmer, discontinuous permafrost landscapes are the ones that have crossed a tipping point and experienced thaw in the historical satellite record[18,50] (including thaw at depths comparable to the channel depth of ~10 m (refs. 18,52)).

Meanwhile, Arctic and sub-Arctic rivers have also experienced a widespread reduction in the frequency and intensity of mechanical ice breakup events[53,54] (Fig. 3f), a perturbation that acts to reduce river migration rates. Although all rivers may be undergoing a similar reduction in ice erosion, this perturbation has the largest relative effect (that is, largest percent change in M_{avg}) for the rivers in the coldest environments, which tend to have slower average migration rates and a larger

https://doi.org/10.1038/s41558-025-02512-w

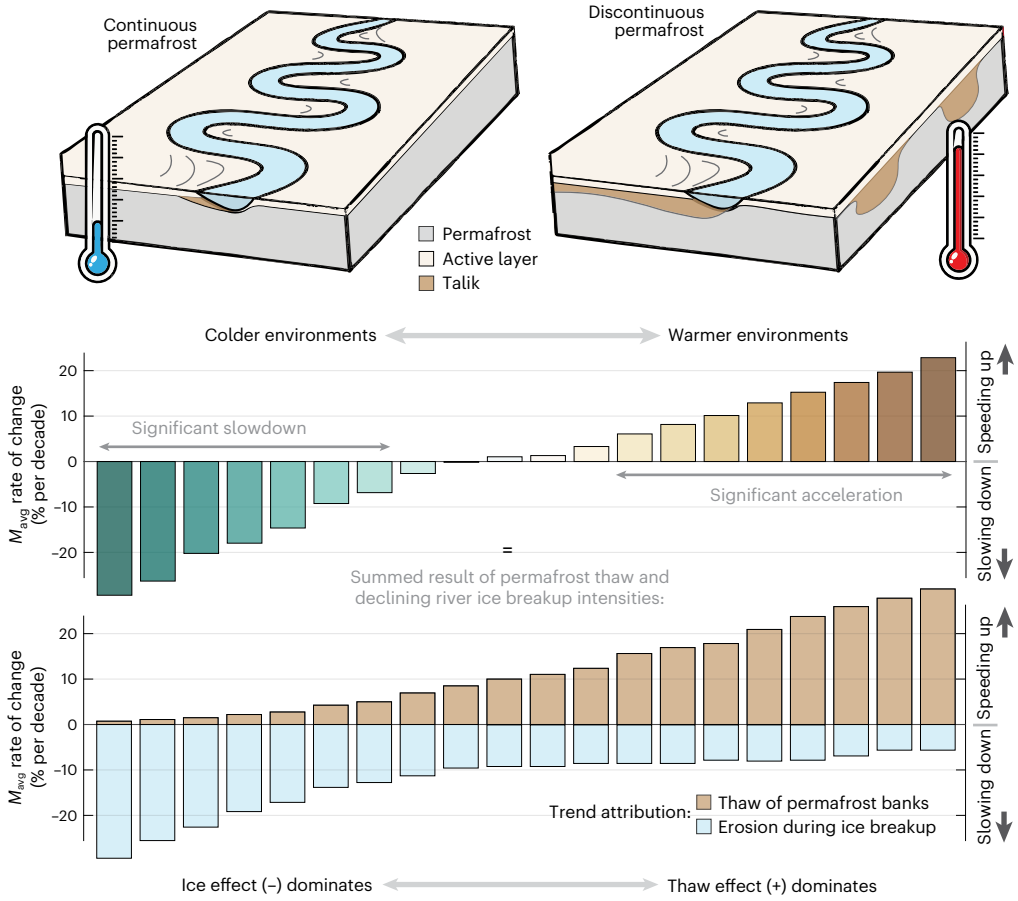

Fig. 6 | A conceptual model to explain the diverging speeding versus slowing trends in Fig. 2c. The rivers that are experiencing a slowdown in river migration tend to be in the coldest environments underlain by continuous permafrost, whereas the rivers experiencing an increase in migration rates tend to be in warmer transitional environments of discontinuous permafrost (Fig. 2d). These warmer environments are more likely to have crossed a tipping point for sub-aerial talik formation[18], causing the fraction of floodplain permafrost coverage to change during the recent satellite record[50] (Supplementary Fig. 27). Meanwhile, Arctic and sub-Arctic rivers have simultaneously experienced a decline in the frequency and intensity of mechanical ice breakup events[31,53,54] (Fig. 3f), a trend that leads to slower erosion rates. The relative balance between these two processes: floodplain permafrost thaw and river-ice breakup, determines where a particular river sits along the spectrum of slowing versus speeding (Fig. 2c).

proportion of their total erosion caused by mechanical ice breakup (Extended Data Tables 1 and 2).

Thus, our observations support the conceptual model in which the diverging speeding versus slowing trends in Fig. 2c reflect the balance between two competing processes: floodplain permafrost thaw and declining river-ice breakup intensities (Fig. 6). Rivers in the coldest environments have not yet experienced substantial permafrost degradation, so the ice effect dominates.

Implications for river migration in a warming Arctic

The quantification of river dynamics in the recent historical record provides constraints to validate models for future river behaviour in the twenty-first century and beyond. Our observations suggest that, as the Arctic warms and landscapes transition from continuous permafrost to discontinuous permafrost to no permafrost[19,20], river migration rates may evolve as a wave that propagates across both space and time. Although the majority of Arctic and sub-Arctic rivers are experiencing a declining intensity of river-ice breakup[31,53,54], only the rivers in transitional permafrost landscapes are currently experiencing the thaw-induced increases in erosion rates[11]. As the Arctic continues to warm[33], the fringe of this permafrost transition zone will propagate into regions that are currently underlain by stable permafrost[18–20], and rivers that have seen declining migration rates in the past 50 years may transition to a state of accelerated riverbank erosion. This transition to faster river migration will affect local infrastructure and communities[4], regional water quality and turbidity[8], and global biogeochemical cycles[2,9].

Online content

Any methods, additional references, Nature Portfolio reporting summaries, source data, extended data, supplementary information, acknowledgements, peer review information; details of author contributions and competing interests; and statements of data and code availability are available at https://doi.org/10.1038/s41558-025-02512-w.

References

1. Hugelius, G. et al. Estimated stocks of circumpolar permafrost carbon with quantified uncertainty ranges and identified data gaps. *Biogeosciences* **11**, 6573–6593 (2014).
2. Lininger, K., Wohl, E., Rose, J. & Leisz, S. Significant floodplain soil organic carbon storage along a large high-latitude river and its tributaries. *Geophys. Res. Lett.* **46**, 2121–2129 (2019).
3. Geyman, E. C. et al. Scaling laws for sediment storage and turnover in river floodplains. *Sci. Adv.* **11**, 8574 (2025).
4. Hjort, J. et al. Degrading permafrost puts Arctic infrastructure at risk by mid-century. *Nat. Commun.* **9**, 5147 (2018).

5. Teufel, B. & Sushama, L. Abrupt changes across the Arctic permafrost region endanger northern development. *Nat. Clim. Change* **9**, 858–862 (2019).
6. Rowland, J. C. et al. Scale-dependent influence of permafrost on riverbank erosion rates. *J. Geophys. Res. Earth Surf.* **128**, e2023JF007101 (2023).
7. Wild, B. et al. Rivers across the Siberian Arctic unearth the patterns of carbon release from thawing permafrost. *Proc. Natl Acad. Sci. USA* **116**, 10280–10285 (2019).
8. Zhang, T. et al. Warming-driven erosion and sediment transport in cold regions. *Nat. Rev. Earth Environ.* **3**, 832–851 (2022).
9. Terhaar, J., Lauerwald, R., Regnier, P., Gruber, N. & Bopp, L. Around one third of current Arctic Ocean primary production sustained by rivers and coastal erosion. *Nat. Commun.* **12**, 169 (2021).
10. Smith, M. I. et al. Mercury stocks in discontinuous permafrost and their mobilization by dynamic erosion and sedimentation in the Yukon River Basin. *Environ. Res. Lett.* **19**, 084041 (2024).
11. Geyman, E. C., Douglas, M. M., Avouac, J.-P. & Lamb, M. P. Permafrost slows Arctic riverbank erosion. *Nature* **634**, 359–365 (2024).
12. Gautier, E. et al. Fifty-year dynamics of the Lena River islands (Russia): spatio-temporal pattern of large periglacial anabranching river and influence of climate change. *Sci. Total Environ.* **783**, 147020 (2021).
13. Ielpi, A., Lapôtre, M. G., Finotello, A. & Roy-Léveillée, P. Large sinuous rivers are slowing down in a warming Arctic. *Nat. Clim. Change* **13**, 375–381 (2023).
14. Wulder, M. A. et al. Fifty years of Landsat science and impacts. *Remote Sens. Environ.* **280**, 113195 (2022).
15. Feng, D. et al. Recent changes to Arctic river discharge. *Nat. Commun.* **12**, 6917 (2021).
16. Douglas, M. M., Dunne, K. B. & Lamb, M. P. Sediment entrainment and slump blocks limit permafrost riverbank erosion. *Geophys. Res. Lett.* **50**, e2023GL102974 (2023).
17. Douglas, M. M., Miller, K. L., Schmeer, M. N. & Lamb, M. P. Ablation-limited erosion rates of permafrost riverbanks. *J. Geophys. Res. Earth Surf.* **128**, e2023JF007098 (2023).
18. Farquharson, L. M., Romanovsky, V. E., Kholodov, A. & Nicolsky, D. Sub-aerial talik formation observed across the discontinuous permafrost zone of Alaska. *Nat. Geosci.* **15**, 475–481 (2022).
19. Smith, S. L., O'Neill, H. B., Isaksen, K., Noetzli, J. & Romanovsky, V. E. The changing thermal state of permafrost. *Nat. Rev. Earth Environ.* **3**, 10–23 (2022).
20. Chadburn, S. et al. An observation-based constraint on permafrost loss as a function of global warming. *Nat. Clim. Change* **7**, 340–344 (2017).
21. Kanevskiy, M. et al. Patterns and rates of riverbank erosion involving ice-rich permafrost (yedoma) in northern Alaska. *Geomorphology* **253**, 370–384 (2016).
22. Fields, J., Kreisler, J., Dethier, E., Perrotti, J. & Renshaw, C. Fluvial erosion linked to warming in the Canadian Arctic. *Commun. Earth Environ.* **6**, 267 (2025).
23. Constantine, J. A., Dunne, T., Ahmed, J., Legleiter, C. & Lazarus, E. D. Sediment supply as a driver of river meandering and floodplain evolution in the Amazon Basin. *Nat. Geosci.* **7**, 899–903 (2014).
24. Gordeev, V. Fluvial sediment flux to the Arctic Ocean. *Geomorphology* **80**, 94–104 (2006).
25. Dethier, E. N., Renshaw, C. E. & Magilligan, F. J. Rapid changes to global river suspended sediment flux by humans. *Science* **376**, 1447–1452 (2022).
26. Sun, X. et al. Changes in global fluvial sediment concentrations and fluxes between 1985 and 2020. *Nat. Sustain.* **8**, 142–151 (2025).
27. Ielpi, A. & Lapôtre, M. G. A tenfold slowdown in river meander migration driven by plant life. *Nat. Geosci.* **13**, 82–86 (2020).
28. Myneni, R. B., Keeling, C., Tucker, C. J., Asrar, G. & Nemani, R. R. Increased plant growth in the northern high latitudes from 1981 to 1991. *Nature* **386**, 698–702 (1997).
29. Chassiot, L., Lajeunesse, P. & Bernier, J.-F. Riverbank erosion in cold environments: review and outlook. *Earth Sci. Rev.* **207**, 103231 (2020).
30. Yang, X., Pavelsky, T. M. & Allen, G. H. The past and future of global river ice. *Nature* **577**, 69–73 (2020).
31. Vandermause, R., Harvey, M., Zevenbergen, L. & Ettema, R. River-ice effects on bank erosion along the middle segment of the Susitna River, Alaska. *Cold Reg. Sci. Technol.* **185**, 103239 (2021).
32. Lininger, K. B. & Wohl, E. Floodplain dynamics in North American permafrost regions under a warming climate and implications for organic carbon stocks: a review and synthesis. *Earth Sci. Rev.* **193**, 24–44 (2019).
33. Post, E. et al. The polar regions in a 2°C warmer world. *Sci. Adv.* **5**, eaaw9883 (2019).
34. Serreze, M. C. & Barry, R. G. Processes and impacts of Arctic amplification: a research synthesis. *Glob. Planet. Change* **77**, 85–96 (2011).
35. Rowland, J. et al. Arctic landscapes in transition: responses to thawing permafrost. *Eos Trans. Am. Geophys. Union* **91**, 229–230 (2010).
36. Pastick, N. J. et al. Distribution of near-surface permafrost in Alaska: estimates of present and future conditions. *Remote Sens. Environ.* **168**, 301–315 (2015).
37. Yan, L. & Roy, D. Improving Landsat Multispectral Scanner (MSS) geolocation by least-squares-adjustment based time-series co-registration. *Remote Sens. Environ.* **252**, 112181 (2021).
38. Sylvester, Z., Durkin, P. & Covault, J. A. High curvatures drive river meandering. *Geology* **47**, 263–266 (2019).
39. Finotello, A. et al. Vegetation enhances curvature-driven dynamics in meandering rivers. *Nat. Commun.* **15**, 1968 (2024).
40. Greenberg, E., Chadwick, A. J. & Ganti, V. A generalized area-based framework to quantify river mobility from remotely sensed imagery. *J. Geophys. Res. Earth Surf.* **128**, e2023JF007189 (2023).
41. Ju, J. & Masek, J. G. The vegetation greenness trend in Canada and US Alaska from 1984–2012 Landsat data. *Remote Sens. Environ.* **176**, 1–16 (2016).
42. Spawn, S. A., Sullivan, C. C., Lark, T. J. & Gibbs, H. K. Harmonized global maps of above and belowground biomass carbon density in the year 2010. *Sci. Data* **7**, 112 (2020).
43. Phillips, C. B. et al. Threshold constraints on the size, shape and stability of alluvial rivers. *Nat. Rev. Earth Environ.* **3**, 406–419 (2022).
44. Partheniades, E. Erosion and deposition of cohesive soils. *J. Hydraul. Div.* **91**, 105–139 (1965).
45. Costard, F., Dupeyrat, L., Gautier, E. & Carey-Gailhardis, E. Fluvial thermal erosion investigations along a rapidly eroding river bank: application to the Lena River (central Siberia). *Earth Surf. Process. Landf.* **28**, 1349–1359 (2003).
46. Dupeyrat, L. et al. Effects of ice content on the thermal erosion of permafrost: implications for coastal and fluvial erosion. *Permafr. Periglac. Process.* **22**, 179–187 (2011).
47. *CRREL Ice Jam Database [Dataset]* (Cold Regions Research and Engineering Laboratory (CRREL), accessed 12 Jan 2025 (2025); https://icejam.sec.usace.army.mil/
48. Anadu, J. et al. *Suspended and Bed Sediment Grain Size Distributions at Three Riverine Sites in the Yukon River Watershed: Alakanuk, Beaver, and Huslia (Alaska) (2018–2023)* (Arctic Data Center, 2025); https://doi.org/10.18739/A22Z12R5X
49. Yoshikawa, K. *Permafrost in Our Time* (Univ. Alaska Fairbanks Permafrost Outreach Center, 2013).

50. Lawrence, D. M., Slater, A. G. & Swenson, S. C. Simulation of present-day and future permafrost and seasonally frozen ground conditions in CCSM4. *J. Clim.* **25**, 2207–2225 (2012).
51. Biskaborn, B. K. et al. Permafrost is warming at a global scale. *Nat. Commun.* **10**, 264 (2019).
52. Batir, J. F., Hornbach, M. J. & Blackwell, D. D. Ten years of measurements and modeling of soil temperature changes and their effects on permafrost in Northwestern Alaska. *Glob. Planet. Change* **148**, 55–71 (2017).
53. Beltaos, S. Threshold between mechanical and thermal breakup of river ice cover. *Cold Reg. Sci. Technol.* **37**, 1–13 (2003).
54. Beck, R. A. et al. Contrasting historical and recent breakup styles on the Meade River of Arctic Alaska in the context of a warming climate. *Am. J. Clim. Change* **2**, 165–172 (2013).
55. Frost, G. V., Bhatt, U. S., Macander, M. J., Hendricks, A. S. & Jorgenson, M. T. Is Alaska's Yukon–Kuskokwim Delta greening or browning? Resolving mixed signals of tundra vegetation dynamics and drivers in the maritime Arctic. *Earth Interact.* **25**, 76–93 (2021).

Methods

Quantifying changes in river migration rates

A note on the non-stationarity of satellite datasets. Across the nine satellites of the Landsat programme (1972 to the present), the spatial resolution has continuously improved from 80-m ground sampling, to 30-m sampling, to 15-m (panchromatic) sampling[14] (Extended Data Fig. 1a). First, we asked whether this steadily improving spatial resolution and associated georeferencing accuracy imparts a methodological bias that makes it appear as though river migration rates have increased or decreased over time, even in the absence of any change. We began with the observation that there are two characteristics that make estimates of Arctic river migration particularly susceptible to this type of artefact:

(1) **Arctic river migration rates hover around the detection limit for Landsat imagery**. River migration may be fast from a geological perspective[3,56], but it is slow from the perspective of decadal-scale satellite missions. For example, in a global-scale meta-analysis, ref. 6 reports average migration rates of Arctic rivers of 3.0 ± 3.4 m yr^{-1} ($\mu \pm 1\sigma$). Assuming this average rate, it takes 27 years (half of the ~50-year satellite record) for a river to erode the distance equivalent to a single 80-m sampling distance from a Landsat MSS sensor[14]. One implication of these slow migration rates is the fact that misplacing the channel bank position at the scale of a single pixel could result in a ~100% increase or decrease in the inferred migration rate.

(2) **Image co-registration errors can masquerade as river migration**. Uncertainty in the channel bank position on the scale of a single pixel is a reasonable expectation given the persistent image georeferencing errors in optical satellite datasets[37]. For example, the MSS data from the Landsat 1–5 satellites (1972–2013)[14], even when processed at the highest level (L1TP; precision and terrain-correction processing), can have misregistration errors on the scale of ~60 m[37]. Crucially, shifts in the channel position resulting from image co-registration errors resemble natural channel migration patterns (Extended Data Fig. 1b,c). The two most widely used methodologies for quantifying river migration from satellite data: (1) using dynamic time warping (DTW) to calculate the displacement of the channel centreline[13,38,39], or (2) calculating pixel-level changes from floodplain to channel or vice versa[40,57], are both susceptible to mistaking image misregistration errors for river migration (Extended Data Fig. 1b,c).

A synthetic experiment to test for methodological bias. We conducted a simple numerical experiment to test whether factors (1) and (2) above might have conspired to produce an apparent change in river migration rates over the past 50 years, even if no such change exists. First, we simulated river migration using a widely used meander model[58]. We simulated 50 years of migration under the null hypothesis of a constant migration rate. At 5-year timesteps (the same timesteps used in previous analyses[13]), we resampled the river planform to a discrete grid of 60 m, 30 m or 15 m, in accordance with the Landsat record shown in Extended Data Fig. 1a. We allowed the river planform to experience a one-half-pixel co-registration error, which is a conservative estimate for Landsat products[37]. Finally, we followed widespread methodology[13,38,39] (Extended Data Fig. 1b) and used dynamic time warping to calculate the migration rates for the river planforms sampled at each 5-year time step. We repeated the simulation $n = 20$ times to generate an ensemble of synthetic observations. The results are shown in Extended Data Fig. 3e. Note how, even though the true (imposed) migration rate is kept constant, the measured migration declines at a rate of ~20% per decade, recreating the findings of ref. 13 (Extended Data Fig. 1a).

A methodology that is robust to changes in image resolution. We developed a method for measuring river lateral migration rate that is robust to changes in image resolution and pixel-scale co-registration errors. We began with the observation that the first-order control on the migration rates of meandering rivers is the channel curvature[38]. For example, in a typical large meandering river, the migration rate may vary from 0 m yr^{-1} at the straightaways to 5 m yr^{-1} at the bends[11,38] (Extended Data Fig. 3b). According to the numerical model of ref. 58 (and consistent with observations of modern rivers[11,38]), the local migration rate is a quasi-linear function of the channel curvature (adjusted for a spatial lag on the order of ~2 channel widths[11,38,58]). The slope of this linear relationship between the lag-adjusted curvature and migration rate is described by an erodibility coefficient, k, with units of m yr^{-1} (Extended Data Fig. 3c).

Thus, the average migration rate of a meandering river can increase in two ways: (1) through an increase in the erodibility coefficient k, and/or (2) through an increase in the average river curvature (for example, associated with increases in sinuosity). For any pair of images, k can be estimated by regressing the local channel migration rate to the lag-adjusted curvature[38] (Extended Data Fig. 3c). Then, the reach-averaged migration rate can be calculated by averaging the product of the erodibility coefficient and the lag-adjusted curvature (see equation (12)). The advantage of calculating river migration rates using this curvature-based approach is that it is less sensitive to co-registration errors. For example, in the synthetic experiment in Extended Data Fig. 3, we find that co-registration errors produce a systematic overestimation of migration rates using the standard dynamic time warping approach[13,38] (Extended Data Fig. 3e), but little to no bias using our proposed curvature-based approach (Extended Data Fig. 3f).

Workflow for satellite data analysis

Landsat timeseries of channel bank positions. The primary data analysed in this study are riverbank positions digitized from Landsat imagery over the 50-year interval from 1972–2022. We used the 10 river reaches digitized from ref. 13, and then added an additional 12 river reaches digitized for this study. The Landsat image IDs for the river reaches analysed in this study are included in Supplementary Table 3. For consistency with the existing dataset from ref. 13, we analysed one cloud-free Landsat image every ~5 years.

Extracting river centrelines from bank positions. We extracted channel centrelines from the positions of the two riverbanks through the following steps (see Supplementary Fig. 1 for a graphical example). First, we linked the two bank edge vectors to make a filled polygon covering the channel. Next, we converted the polygon into a gridded binary mask. Next, we skeletonized the binary mask using the bwmorph tool in Matlab. Skeletonization repeatedly removes the pixels on the boundaries of the objects (in this case, the channel mask) until the object is only one-pixel wide. The result is a binary image with a single line (one-pixel thick) that defines the middle of the channel mask. Next, we converted the centreline from a raster (gridded mask) to a vector of ordinated (x,y) coordinates, arranged from upstream to downstream. We resampled the centreline path to a uniform spacing of $\Delta x = W/10$, where W is the average channel width.

Quantifying river migration through DTW. We followed refs. 38,39,59 and others to measure channel migration using DTW. We implemented DTW in Matlab using the function dtw. DTW stretches the input vectors or matrices (x and y) into a common set of instants such that the total (summed) Euclidean distances between the matched points are the smallest. In other words, the DTW algorithm seeks to minimize the total distance between the two datasets rather than the distance between any individual corresponding pair of matched data points. A graphical example of the DTW approach is shown in Supplementary Fig. 3.

Measuring river curvature. We followed ref. 38 and smoothed the channel centrelines using a Savitsky–Golay filter (with a frame length

of 33 pixels) and then computed the curvature using the standard formulation in Cartesian coordinates:

$$C = \frac{x'y'' - y'x''}{(x'^2 + y'^2)^{3/2}} \quad (5)$$

where x' and x'' are the first and second-order derivatives in x, and y' and y'' are the first and second-order derivatives in y. The derivatives were computed numerically using the finite central difference formulation.

Linking river curvature to migration through convolutional models. River curvature must be sustained for some distance so that the high-velocity filament of flow in the river channel will be displaced towards the outer bend, increasing the local velocity gradient and therefore the shear stress on the outer bank[60]. This cumulative behaviour of river curvature is captured empirically/phenomenologically by convolutional models such as the model of ref. 58. The bank migration rate, $M(s)$, is described as:

$$M(s) = \Omega M_0(s) + \left(\Gamma \int_0^\infty M_0(s-\zeta)G(\zeta)d\zeta\right)\left(\int_0^\infty G(\zeta)d\zeta\right)^{-1} \quad (6)$$

where s is the along-river coordinate system (longitudinal distance), ζ is the distance upstream from the point of interest, and $G(\zeta)$ is a weighting function that decays exponentially upstream from the point of interest:

$$G(\zeta) = e^{-\alpha\zeta} \quad (7)$$

The α term in equation (7) controls the rate of decay of the influence of the upstream curvature, and it can be parameterized as a function of the friction factor, C_f (dimensionless) and the water depth, H (m)[38,58]:

$$\alpha = 2C_f/H \quad (8)$$

The term $M_0(s)$ represents what ref. 58 refers to as the 'nominal' migration rate; that is, the rate that would be observed if migration were only a function of local curvature. The simplest functional dependence for $M_0(s)$ is[58]:

$$M_0(s) = k\left(\frac{W}{R}\right) \quad (9)$$

where k (m yr^{-1}) is a migration rate constant, W (m) is the channel width, and R (m) is the local radius of curvature. We refer to the dimensionless ratio W/R as the 'local normalized curvature'. In equation (6), Ω and Γ are constants (−1 and 2.5, respectively)[58].

The intuition underlying the ref. 58 model (equation (6)) is that river migration rate depends not only on the local curvature, but also the river curvature upstream of the point of interest. However, the influence of the neighbouring curvature declines as you move farther from the point of interest. The dimensionless 'lag-adjusted curvature' (C_l) can be defined using the convolutional formulation of ref. 58 (equations (6)–(9)) as:

$$C_l = \Omega\left(\frac{W}{R}\right) + \left(\Gamma \int_0^\infty \left(\frac{W}{R}\right)(s-\zeta)G(\zeta)d\zeta\right)\left(\int_0^\infty G(\zeta)d\zeta\right)^{-1}. \quad (10)$$

Equation (10) simply modifies the local normalized curvature (W/R) by the weighting function $G(\zeta)$ that decays exponentially upstream from the point of interest. Based on equation (6), the channel migration rate, M, is a simple linear function of the lag-adjusted dimensionless curvature:

$$M = kC_l \quad (11)$$

where k (m yr^{-1}) is the same migration rate constant as in equation (9). In Fig. 2b, we computed the lag-adjusted curvature (C_l) (equation (10)) using measurements of river width and river curvature, following the methodology of ref. 38. We then compared C_l to the observed migration rates to quantify k. The quantity k conveys how fast river migration proceeds for a given amount of river curvature. This parameter thereby removes the first-order control of river geometry (curvature) in setting local river migration rates[38].

We computed the reach-averaged migration rate, M_{avg} as the spatial average of kC_l (equation (11)) along the studied river reach:

$$M_{avg} = \frac{1}{L}\int_0^L kC_l(s)ds \quad (12)$$

where s denotes the position along the streamwise coordinate system, L is the length of the river reach, k is the reach-specific estimate of the erodibility coefficient (that is, the slope of the trends in Fig. 2b), and $C_l(s)$ is the lag-adjusted dimensionless curvature.

Filtering datasets that lack a strong curvature–migration relationship. Two of the rivers used in ref. 13 (the Stewart and Kobuk Rivers) lack a robust relationship between migration rate and curvature, at least when using the (spatially coarse) input datasets of digitized bank positions from Landsat imagery. We quantified the robustness of the curvature versus migration rate relationship using the R^2 value of the lag-adjusted curvature (C_l) versus local migration rate (M) cross-plot similar to the ones shown in Fig. 2b. Both the Stewart and Kobuk Rivers have $R^2 < 0.5$, meaning that the integrated upstream curvature describes less than half of the variance in the observed migration rates of those rivers. Since we lacked confidence in our ability to constrain k for those rivers, we excluded the Stewart and Kobuk from our analysis (Fig. 2).

Searching for evidence of bias. Recall that the methodological bias imparted by directly matching riverbank positions over time (Extended Data Fig. 1b,c) acts in the direction that rivers with lower true migration rates are more likely to appear to be slowing down across the historical satellite record. A potential criticism of our methodology is that it could have the opposite tendency. That is, greater noise (scatter) in the curvature versus migration rate regression resulting from image co-registration errors (Extended Data Fig. 3d) could result in an underestimation of k, leading to an (erroneous) increase in the inferred k over the Landsat observational record. We took steps to avoid this behaviour. First, we calculated k through a total least squares (TLS) regression rather than an ordinary least squares (OLS) regression, to minimize the extent to which noise on the y axis of Extended Data Fig. 3d suppresses the estimate of k. Our synthetic experiments revealed only a small trend in the inferred k across the Landsat record (Extended Data Fig. 3f), a trend whose magnitude is approximately 7× smaller than the default approach illustrated in Extended Data Fig. 3e. Second, we also examined the results in Fig. 2 for the fingerprints of a systematic bias. In particular, the bias we were worried about introducing with our methodology would cause rivers with lower migration rates to be more likely to appear to be speeding up. Instead, the data in Fig. 2c showed the opposite trend; rivers with slower average migration rates tended to be slowing down, whereas rivers with faster average migration rates tended to be accelerating.

Applying a mechanistic model for riverbank erosion

We built on refs. 11,16 and used a model in which the erosion of permafrost riverbanks is governed by the dual constraints of thaw and entrainment. We describe the model introduced in the main text in more detail here. The rate of thaw-limited erosion (E_{thaw}, [$L\,T^{-1}$]) is expressed as[16,45,46]:

$$E_{thaw} = \frac{A\mathrm{Pr}^{\alpha}\mathrm{Re}^{\beta}\kappa_w(T_w - T_f)}{H\rho_b(L_f + c_p(T_f - T_i))} \quad (13)$$

where A, α and β are (dimensionless) empirical coefficients, $\mathrm{Pr} = \nu/\chi$ is the Prandtl number, ν ($m^2\ s^{-1}$) is the kinematic viscosity of water, χ ($m^2\ s^{-1}$) is the thermal diffusivity of water, $\mathrm{Re} = HU/\nu$ is the Reynolds number, U ($m\ s^{-1}$) is the mean flow velocity, κ_w ($W\ m^{-1}\ °C^{-1}$) is the thermal conductivity of water, T_w is the river water temperature (°C), T_f is the freezing point of water (°C), T_i is the initial temperature of the permafrost riverbank (°C), H (m) is the river flow depth, ρ_b ($kg\ m^{-3}$) is the bulk density of the permafrost riverbank, L_f ($J\ kg^{-1}$) is the permafrost latent heat of fusion (calculated as $L_f = f_{ice}L_{ice}$, where f_{ice} ($kg\ kg^{-1}$) is the mass fraction of water ice in the permafrost riverbank and L_{ice} ($J\ kg^{-1}$) is the latent heat of fusion for water ice) and c_p ($J\ kg^{-1}\ °C^{-1}$) is the permafrost heat capacity. Note that we define E_{thaw} only for $T_w \geq 0$.

We represent entrainment-limited erosion using the common threshold formulation[44]:

$$E_{ent} = \frac{B}{\rho_b f_{sed}}\left(\frac{\tau_{bank}}{\tau_{crit}} - 1\right)^n \quad (14)$$

where τ_{bank} (Pa) is the shear stress on the bank, τ_{crit} (Pa) is the critical shear stress required to entrain bank sediment, $f_{sed} = 1 - f_{ice}$ (dimensionless) is the mass fraction of sediment, and B ($kg\ m^{-2}\ s^{-1}$) and n (dimensionless) are empirical coefficients[16,44]. To solve for E_{ent}, we used the following set of assumptions. First, we needed a method to partition the total fluid shear stress in the channel (τ) between the channel bed and the bank[61]. To first order, the bed and bank stress partitioning depends on the relative roughness of the two surfaces and the channel width-to-depth ratio[61–64]. For simplicity, we let the shear stress on the bank (τ_{bank}) follow the near-threshold '$(1+\epsilon)$' model of refs. 43,65:

$$\tau_{bank} = \left(\frac{1}{1+\epsilon}\right)\tau_{bed} \quad (15)$$

where $\epsilon = 0.2$ (refs. 43,65). The shear stress on the bed can be related to the flow velocity using a canonical flow-resistance equation[43]:

$$\tau_{bed} = \rho_w C_f U^2 \quad (16)$$

where ρ_w ($kg\ m^{-3}$) is the density of water. Equation (16) is based on the relationship between the cross-sectionally averaged flow velocity, U, and the shear velocity, u_*, through a dimensionless friction coefficient, C_f:

$$U = \frac{1}{\sqrt{C_f}}u_* \quad (17)$$

where u_* is defined as:

$$u_* = \sqrt{\tau_{bed}/\rho_w} \quad (18)$$

Combining equation (14) with equations (15) and (16), we arrived at the expression:

$$E_{ent} = \frac{B}{\rho_b f_{sed}}\left(\frac{\rho_w C_f U^2}{(1+\epsilon)\tau_{crit}} - 1\right)^n \quad (19)$$

We define equation (19) only for $E_{ent} \geq 0\ m\ yr^{-1}$. See Supplementary Table 2 for the list of parameter values used in equations (13)–(19). See Section 3 for a discussion of the model implementation and sensitivity analysis.

Lastly, we must account for the fact that Arctic rivers, particularly those in discontinuous permafrost landscapes, variably encounter riverbanks that are frozen (permafrost) and unfrozen (non-permafrost)[11]. Permafrost thaw, including sub-aerial talik formation[18], will cause the proportion of unfrozen riverbanks to increase over time. To account for this spatial heterogeneity of permafrost versus non-permafrost riverbanks in our model, we incorporated the dimensionless parameter P_t, which is labelled as 'Prob. talik' in Fig. 3i.

P_t varies from 0 to 1, and it represents the fraction of the eroding riverbanks that are non-permafrost. For the non-permafrost riverbanks (with a proportion P_t), we applied the entrainment-only erosion model (equation (2); Fig. 4b,c). For the permafrost riverbanks (which constitute the proportion $(1 - P_t)$ of all eroding riverbanks), we applied the dual thaw- and entrainment-limited model (argmin$\{E_{ent}, E_{thaw}\}$; Fig. 4d). We estimated P_t for each site using the permafrost map of ref. 36 (see Supplementary Fig. 28).

The data-driven P_t estimate shown in Supplementary Fig. 28 (and in Fig. 3i of the main text) represents a quasi-static historical value (with a representative age that matches when the $n \approx 17{,}000$ permafrost probe observations that serve as the training data for the permafrost map of ref. 36 were acquired). For the erosion budget and trend attribution analysis shown in Fig. 5, we were interested in understanding whether P_t must have changed over the recent historical record (1985–2025) to explain the observed trends in channel migration rates. Therefore, we added one final parameter to the model (R_{thaw}, [$\%\ yr^{-1}$]), which represents the floodplain thaw rate (that is, the change in P_t per year). Both observations[18,20] and models[50,66,67] indicated that permafrost degradation has begun to occur in the past ~4 decades (Supplementary Fig. 27), including to depths of ~10 m that are representative of the channel depths[18,52]. However, so far, permafrost degradation has primarily occurred in landscapes that are at the transition of permafrost stability (that is, those that currently have discontinuous or sporadic permafrost)[18,19,68]. In contrast, landscapes where the mean annual ground temperature is very cold (for example, <−10 °C) are less likely to experience major changes in permafrost abundance for the next several decades[18–20]. This varied sensitivity across space could help explain why rivers in discontinuous permafrost landscapes have exhibited a statistically significant increase in river migration rates over the past 50 years, whereas rivers in continuous permafrost landscapes and non-permafrost landscapes have not (Fig. 2). In the historical trend attribution analysis in Fig. 5, we found that the migration rate observations at the colder Yukon River site (Beaver, Alaska) are well explained by an average $R_{thaw} = 0\%\ yr^{-1}$ over the 1985–2025 historical record, whereas the migration rate observations at the warmer Koyukuk River site (Huslia, Alaska) are better explained by a $1\%\ yr^{-1}$ reduction in P_t over the 1985–2025 historical record. These parameter inversions are consistent with models of permafrost degradation in transitional permafrost environments[50].

Estimated changes in river migration rates

Extended Data Table 1 summarizes the site information and the temporal trends in migration rate for the investigated river reaches from Fig. 2. Extended Data Table 2 provides additional environmental data (including the floodplain aboveground biomass densities, the NDVI trends, the permafrost abundance and the mean annual temperature) for the studied reaches.

Evaluating potential drivers of Arctic river change

Water discharge. Streamflow records for the investigated rivers (Fig. 2a) are available from the US Geological Survey and the National Hydrological Service of Canada (Supplementary Figs. 13 and 14). We found that, for the 9 study sites with streamgauge records containing at least 30 years of data, the mean discharge trend is just +2.7% per decade (95% confidence interval: +1.5 to +3.9% per decade) (Fig. 3a). We did not observe major trends in the magnitude of the peak annual discharge, nor in the magnitude of discharge that occurs in the warmest months of the year (July–August), when sluggish water flow is hypothesized to be the principal factor limiting erosion[11,16] (Fig. 5). To expand our analysis beyond the $n = 9$ river reaches with long in situ observational records, we used precipitation data from ERA5 (ref. 69) weather reanalysis to estimate the hydrological forcing of each river

basin from 1972 to the present (Supplementary Figs. 19 and 20). The ERA reanalysis suggests that total annual precipitation has not changed significantly across the study region. The 95% confidence interval for precipitation change averaged across all study sites is −2.8 to +3.5% per decade. Moreover, none of the individual reaches exhibited statistically significant declines or increases (Supplementary Fig. 20). Put together, these observations suggest that changing water discharge is unlikely to be a dominant and widespread driver of accelerating or decelerating Arctic river migration rates, at least not in the past 50 years.

Sediment loads. Arctic rivers have been hypothesized to become hotspots of increased sediment transport in the coming century[8,70]. Existing models[71] suggest that, for every 2 °C increase in mean annual temperature, Arctic river sediment loads may increase by ~30%. However, observations from the satellite historical record so far have not found a major change in Arctic river sediment loads at a regional scale[25,26] (although there is evidence of sediment loads increasing locally[72,73]). Here we leveraged a dataset of remote-sensing-derived suspended sediment concentrations for the period 1985–2020[26]. We analysed the $n = 278$ river reaches from Arctic and sub-Arctic Alaska and NW Canada included in the dataset of ref. 26 (Supplementary Fig. 21) and found that there is no statistically significant trend in the suspended sediment concentration over time (Fig. 3b). In other words, higher sediment loads from thawing Arctic catchments, for example, those driven by increases in the number of retrogressive thaw slumps[72,73], may load Arctic river systems with more sediment in the future (and thereby drive faster river migration[23]). However, such a change is not evident for the analysed rivers in the satellite record of 1985–2020, and therefore is unlikely to be driving the acceleration or slowdown patterns shown in Fig. 2.

River temperatures. Water temperatures could influence river migration rates because, in places where the riverbank is frozen (permafrost), erosion of the riverbank requires sufficient heat transfer from the river water to melt the pore ice cementing the sand particles together[16,17]. This heat flux scales with the temperature difference between the river water and the frozen bank[17], so higher river temperatures cause faster rates of thaw-limited erosion[17]. Unfortunately, there are few long-term records of river water temperature[74,75], although remote-sensing-based analyses could fill this void in the future. We analysed two of the longest-running Arctic river temperature records that we are aware of: the Yukon River in Alaska and the Lena River in Siberia[74,75]. Neither record shows a statistically significant trend over time (Fig. 3c). Moreover, mechanistic models validated against observational data[11,16] suggest that erosion of permafrost riverbanks is only weakly sensitive to summertime water temperature, since the time of year when water temperatures are significantly above freezing (July–August) are times when riverbank erosion is limited by flow velocity rather than water temperature (Fig. 5a–c).

Permafrost thaw on floodplains. Another explanation for accelerating bank erosion is that top–down and lateral permafrost thaw driven by atmospheric warming[19,20] and hydrological pumping through the subsurface floodplain causes riverbanks to thaw[18]. Thawed riverbanks can be structurally destabilized[21], and they become more erodible because they are no longer subject to the dual constraint of thaw and entrainment[11,16] (Fig. 5d). Global estimates[20] suggest that permafrost coverage may reduce by ≥40% as global air temperatures rise by 2 °C. Networks of permafrost monitoring stations provide constraints on changing ground temperatures, active layer thicknesses, and ultimately the transformation from perennially frozen to seasonally frozen ground[18]. Figure 3c shows mean annual ground temperatures for seven such sites as an example (see Supplementary Fig. 26 for additional sites). All sites show a statistically significant warming trend. In other words, of the measurements of Arctic environmental change, one of the most decisive is that of permafrost warming, degradation and thaw[18–20,51].

Shrubification of riverbanks. Initial observations of the 'greening of the Arctic'[28] have been followed in recent years by several observations of widespread Arctic 'browning'[76]. Remote sensing datasets increasingly support the understanding that the Arctic consists of a patchwork of contrasting greening versus browning trends, which vary across space and time[77] (Supplementary Fig. 29). Of the $n = 20$ river reaches investigated in Fig. 2, $n = 7$ reaches have floodplains that have exhibited significant greening trends over the period 1984–2012[41], $n = 2$ have floodplains that have exhibited significant browning trends, and $n = 11$ have exhibited no statistically significant trend (Supplementary Figs. 30 and 31). Figure 3e shows an illustration of annually resolved greening/browning timeseries for the Yukon-Kuskokwim Delta[55]. Not only is the decadal trend small relative to the amplitude of the interannual variability, but also the inferred trend depends on the satellite sensor[55]. Figure 3e illustrates why a single image pair from the start and end of a multidecade timeseries[13] is insufficient to robustly capture long-term greening versus browning trends[77]. We found that when we use greening/browning trends inferred from dozens of satellite observations over the interval 1984–2012 (averaging ~40 observations per site)[41], there is no correlation between which rivers traverse landscapes that have been greening versus browning and which rivers have been speeding up versus slowing down (Fig. 2d and Supplementary Fig. 31).

River-ice breakup. Several studies have used global and local observations to quantify significant changes in the occurrence of river ice[30,54,78] over the past several decades. Most analyses focus on changes in the duration (number of days per year) when rivers are frozen. For example, ref. 30 found that, for every 1 °C increase in global mean air temperature, the mean seasonal river ice duration has decreased by 6.1 ± 0.1 days. However, more important to bank erosion is not the duration of the winter river-ice season, but rather the style and intensity of river-ice breakup in the spring[29,31,53,54,78]. Broadly, river-ice breakup events fall into one of two categories: (1) thermal (over-mature) breakup and (2) mechanical (pre-mature) breakup[53]. Thermal breakup refers to years when the river-ice cover melts and deteriorates in place before runoff from the uplands (from snowmelt or precipitation) causes the river discharge to increase[53]. In these years, the river ice disintegrates and flows out to sea under a modest current, causing little to no ice jamming. In contrast, mechanical (pre-mature) ice breakup occurs when rapid runoff from the uplands causes the river discharge to spike while the river-ice cover is still thick and strong. In these years, large hydraulic forces are required to lift and break the river-ice, and the ice fragments can get imbricated and piled-up against the river banks and bed, causing ice jams[53,78]. Case studies from individual Arctic rivers[31] suggest that mechanical breakup events can constitute ≥60% of the total annual erosion in a few-day period, whereas thermal breakup events result in little or no bank erosion[31]. In addition, some reports suggest that there has been a persistent shift over the past 50 years from breakup styles that are predominantly mechanical to breakup styles that are predominantly thermal[54]. To quantify this trend on a large scale, we leveraged the Ice Jam Database maintained by the Cold Regions Research and Engineering Laboratory (CRREL)[47] (Supplementary Figs. 32 and 33). Using documented ice jams as a proxy for a breakup style that is predominantly mechanical rather than thermal[53], we found that ice jam frequencies have decreased over the past several decades at a rate of −26 ± 10% per decade (Fig. 3f). The significant decline in ice jams provides a viable explanation for the observed slowdown of some Arctic rivers (Figs. 2 and 6).

Data availability

The database of riverbank boundaries digitized from Landsat satellite imagery and used to reconstruct river migration rates over the

period 1972–2020 is available on Zenodo at https://doi.org/10.5281/zenodo.15002956 (ref. 79). Note that this study builds on an existing dataset of bank positions of $n = 10$ Arctic river reaches digitized in ref. 13. This original dataset is also available on Zenodo at https://doi.org/10.5281/zenodo.7556050 (ref. 80). The Landsat image archives are accessible through the USGS EarthExplorer (https://earthexplorer.usgs.gov/). The Supporting Information includes a complete list of Landsat scene IDs utilized in this study. The global aboveground biomass map from ref. 42 is available at https://doi.org/10.3334/ORNLDAAC/1763. The NDVI trend (greening versus browning) statistics from ref. 41 are available at https://doi.org/10.3334/ORNLDAAC/1576. Streamflow data are available from the USGS National Water Dashboard (https://dashboard.waterdata.usgs.gov/app/nwd/en/) and the National Hydrological Service of Canada (https://wateroffice.ec.gc.ca/). The remote-sensing-derived estimates of riverine suspended sediment concentrations from ref. 26 are available at https://figshare.com/s/dde3bffd8e12227e2b26. The permafrost mean annual ground temperature observations are available from ref. 51 at https://doi.org/10.1594/PANGAEA.930669. The Cold Regions Research and Engineering Laboratory (CRREL) Ice Jam Database[47] is available at https://icejam.sec.usace.army.mil/. The Alaska permafrost map of ref. 36 is available at https://doi.org/10.5066/F7C53HX6.

Code availability

The code used to perform this analysis is archived on Zenodo at https://doi.org/10.5281/zenodo.15002956 (ref. 79).

References

56. Straub, K. M., Duller, R. A., Foreman, B. Z. & Hajek, E. A. Buffered, incomplete, and shredded: the challenges of reading an imperfect stratigraphic record. *J. Geophys. Res. Earth Surf.* **125**, e2019JF005079 (2020).
57. Rowland, J. C. et al. A morphology independent methodology for quantifying planview river change and characteristics from remotely sensed imagery. *Remote Sens. Environ.* **184**, 212–228 (2016).
58. Howard, A. D. & Knutson, T. R. Sufficient conditions for river meandering: a simulation approach. *Water Resour. Res.* **20**, 1659–1667 (1984).
59. Donovan, M., Belmont, P. & Sylvester, Z. Evaluating the relationship between meander-bend curvature, sediment supply, and migration rates. *J. Geophys. Res. Earth Surf.* **126**, e2020JF006058 (2021).
60. Furbish, D. J. River-bend curvature and migration: how are they related? *Geology* **16**, 752–755 (1988).
61. Vanoni, V. A. & Brooks, N. H. *Laboratory Studies of the Roughness and Suspended Load of Alluvial Streams* (California Institute of Technology Sedimentation Laboratory, 1957).
62. Kean, J. W. & Smith, J. D. in *Riparian Vegetation and Fluvial Geomorphology* (eds Bennett, S. J. & and Simon, A.) 237–252 (American Geophysical Union, 2004).
63. Li, T., Venditti, J. G., Rennie, C. D. & Nelson, P. A. Bed and bank stress partitioning in bedrock rivers. *J. Geophys. Res. Earth Surf.* **127**, e2021JF006360 (2022).
64. Ferguson, R. I., Hardy, R. J. & Hodge, R. A. Flow resistance and hydraulic geometry in bedrock rivers with multiple roughness length scales. *Earth Surf. Process. Landf.* **44**, 2437–2449 (2019).
65. Parker, G. Self-formed straight rivers with equilibrium banks and mobile bed. Part 2. The gravel river. *J. Fluid Mech.* **89**, 127–146 (1978).
66. Lawrence, D. M. & Slater, A. G. A projection of severe near-surface permafrost degradation during the 21st century. *Geophys. Res. Lett.* **32**, L24401 (2005).
67. Peng, X. et al. Active layer thickness and permafrost area projections for the 21st century. *Earths Future* **11**, e2023EF003573 (2023).
68. Jorgenson, M. T. et al. The roles of climate extremes, ecological succession, and hydrology in repeated permafrost aggradation and degradation in fens on the Tanana Flats, Alaska. *J. Geophys. Res. Biogeosci.* **125**, e2020JG005824 (2020).
69. Hersbach, H. et al. The ERA5 global reanalysis. *Q. J. R. Meteorol. Soc.* **146**, 1999–2049 (2020).
70. Li, D. et al. Exceptional increases in fluvial sediment fluxes in a warmer and wetter High Mountain Asia. *Science* **374**, 599–603 (2021).
71. Syvitski, J. P. Sediment discharge variability in Arctic rivers: implications for a warmer future. *Polar Res.* **21**, 323–330 (2002).
72. Kokelj, S. V. et al. Thawing of massive ground ice in mega slumps drives increases in stream sediment and solute flux across a range of watershed scales. *J. Geophys. Res. Earth Surf.* **118**, 681–692 (2013).
73. Erikson, C. M., Dethier, E. N. & Renshaw, C. E. Seasonal dynamics of a coupled hillslope–river system in the Arctic revealed by semi-automated satellite image analysis. *Remote Sens. Environ.* **328**, 114883 (2025).
74. Biela, V. R. et al. Evidence of prevalent heat stress in Yukon River Chinook salmon. *Can. J. Fish. Aquat. Sci.* **77**, 1878–1892 (2020).
75. Chalov, S. et al. Climate change impacts on streamflow, sediment load and carbon fluxes in the Lena River delta. *Ecol. Indic.* **157**, 111252 (2023).
76. Phoenix, G. K. & Bjerke, J. W. Arctic browning: extreme events and trends reversing Arctic greening. *Glob. Change Biol.* **22**, 2960–2962 (2016).
77. Myers-Smith, I. H. et al. Complexity revealed in the greening of the Arctic. *Nat. Clim. Change* **10**, 106–117 (2020).
78. Beltaos, S. & Burrell, B. C. Effects of river-ice breakup on sediment transport and implications to stream environments: a review. *Water* **13**, 2541 (2021).
79. Geyman, E. C. & Lamb, M. P. Are Arctic rivers speeding up or slowing down? Riverbank positions and migration rates of rivers in Alaska and Arctic Canada (1972–2020). *Zenodo* https://doi.org/10.5281/zenodo.15002956 (2025).
80. Ielpi, A., Lapôtre, M. G. A., Finotello, A. & Roy-Léveillée, P. Data for Ielpi et al.'s manuscript "Large sinuous rivers are slowing down in a warming Arctic". *Zenodo* https://doi.org/10.5281/zenodo.7556050 (2023).

Acknowledgements

We thank the Huslia, Beaver and Alakanuk Tribal and Village Councils for river and land access, and S. Huffman, D. Dayton, C. Wiehl, K. Vanderpool, R. Williams, T. Hamilton and the Yukon River Inter-Tribal Watershed Council for logistical support. The photo in Fig. 1d was provided by T. Hamilton on behalf of the Alakanuk Tribal IGAP. This work was supported by NSF Award 2127442 and Caltech's Resnick Sustainability Institute. E.C.G. was supported by the NSF Graduate Research Fellowships Program and the Fannie and John Hertz Foundation.

Author contributions

E.C.G. and M.P.L. designed the study. E.C.G. performed the data analysis and the original drafting of the text, with inputs from M.P.L. E.C.G. and M.P.L. revised the text.

Competing interests

The authors declare no competing interests.

Additional information

Extended data is available for this paper at https://doi.org/10.1038/s41558-025-02512-w.

Supplementary information The online version contains supplementary material available at https://doi.org/10.1038/s41558-025-02512-w.

Correspondence and requests for materials should be addressed to Emily C. Geyman.

Peer review information *Nature Climate Change* thanks Jordan Fields, Marisa Repasch and the other, anonymous, reviewer(s) for their contribution to the peer review of this work.

https://doi.org/10.1038/s41558-025-02512-w

Extended Data Table 1 | Summary of channel migration rate trends and environmental parameters for the n = 20 sites shown in Fig. 2

River	Lat.	Lon.	W [m]	k [m/yr]	M_{avg} [m/yr]	R^2	k trend [%/decade]	M_{avg} trend [%/decade]	NDVI trend [units per decade]	AGB [Mg/ha]	MAT [°C]	PF [%]
Alagnak	59.052	−156.624	120	3.0	1.6	0.77	11.1±6.0	15.8±5.1	0.024	1.8	2.1	8
Big	72.469	−124.322	100	9.2	2.0	0.79	12.0±7.8	3.3±5.2	0.010	0.8	−13.7	-
Ikpikpuk	70.075	−154.676	140	12.8	2.7	0.76	1.6±3.4	1.0±3.2	−0.004	1.7	−10.6	100
Kokolik	69.759	−162.682	110	2.9	1.1	0.78	−14.3±7.3	−18.0±7.1	0.008	2.3	−9.4	91
Koyukuk-1	65.775	−156.417	330	6.3	2.7	0.89	2.0±3.1	6.1±3.5	0.000	8.1	−3.1	50
Koyukuk-2	65.489	−156.395	320	5.6	2.7	0.88	10.3±3.5	13.7±4.0	0.007	12.4	−3.2	43
Koyukuk-3	65.537	−156.837	310	6.6	2.4	0.75	17.3±6.0	16.3±6.7	0.004	9.7	−3.2	50
Koyukuk-4	65.461	−157.344	260	4.9	2.5	0.88	11.4±4.5	15.2±5.5	0.004	7.4	−3.4	51
Kuparuk	70.058	−149.230	120	3.2	0.9	0.83	12.7±4.3	14.4±4.4	0.015	1.5	−10.8	100
Kuskokwim	61.527	−160.215	550	4.1	1.9	0.73	−11.2±4.1	−9.2±4.6	0.011	2.8	−0.7	20
Mackenzie	68.230	−134.381	1000	11.2	5.7	0.82	−2.1±4.8	−2.6±6.4	0.012	19.9	−8.3	-
Nushagak	58.970	−157.725	190	3.5	1.2	0.87	−1.3±5.7	1.3±7.6	0.011	2.5	1.6	0
Porcupine	66.778	−144.280	280	6.7	2.6	0.88	−13.1±3.1	−6.9±4.1	−0.018	17.6	−4.4	38
Portage	58.973	−157.670	180	4.0	2.0	0.8	6.6±6.0	7.2±6.5	0.013	2.5	1.6	0
Slave	60.742	−112.971	710	4.6	1.8	0.74	−0.2±1.1	−0.2±1.1	0.000	32.4	−2.2	-
Squirrel	67.094	−160.620	110	2.4	0.9	0.77	−18.2±7.8	−20.2±8.4	0.022	4.8	−6.2	73
Tanana	64.896	−149.331	500	4.9	2.4	0.73	6.3±6.9	17.7±9.6	−0.025	14.8	−2.1	50
Yukon-Beaver	66.237	−147.962	800	4.2	2.8	0.82	−12.9±5.2	−14.6±5.9	−0.002	17.4	−4.0	49
Yukon-HW1	68.166	−145.522	100	1.4	0.6	0.69	−22.4±6.9	−29.3±6.4	0.003	2.3	−10.8	82
Yukon-HW2	68.388	−145.221	80	1.4	0.8	0.66	−32.8±7.9	−29.4±8.0	-0.003	2.8	−11.4	73

W refers to the channel width, *k* refers to the migration rate coefficient (see Extended Data Fig. 3c), and R^2 refers to the variance reduction of the relationship between lag-adjusted curvature and migration rate (see Fig. 2b). The *k* and M_{avg} trends are both calculated for the period 1972-2020 (Fig. S5). Typically, the *k* and M_{avg} trends are similar (see Fig. S12), but they can differ because M_{avg} is calculated as the reach-averaged product of *k* and the lag-adjusted channel curvature. Therefore, changes in channel curvature (for example, due to cutoff events or other changes in the average sinuosity of the reach) can cause the two metrics to diverge. The NDVI trend metric is based on the 50th percentile of the NDVI trend (1984-2012) from ref. 41 in the floodplain along the river reach. The above-ground biomass (AGB) estimate uses the dataset of ref. 42. The mean annual temperature (MAT) column uses the ERA reanalysis 2 m air temperature[69], calculated over the interval 1972-2020. The PF column lists the 50th percentile of the permafrost probability in the floodplain along the river reach, using the permafrost map of ref. 36.

https://doi.org/10.1038/s41558-025-02512-w

Extended Data Table 2 | An extension of Extended Data Table 1 listing the variability in floodplain above-ground biomass (AGB), NDVI trend, and permafrost (PF) abundance for each river reach

River	AGB [50th] [Mg/ha]	AGB [25th] [Mg/ha]	AGB [75th] [Mg/ha]	NDVI trend per dec. [50th]	NDVI trend per dec. [25th]	NDVI trend per dec. [75th]	PF [50th] [%]	PF [25th] [%]	PF [75th] [%]	MAT [°C]	MAT trend [°C/dec.]	MAT trend 1σ [°C/dec.]
Alagnak	1.8	1.6	2.0	0.024	0.006	0.040	8	0	17	2.1	0.49	0.01
Big	0.8	0.4	1.2	0.010	0.002	0.021	-	-	-	−13.7	0.54	0.01
Ikpikpuk	1.7	1.4	2.0	−0.004	−0.013	0.004	100	100	100	−10.6	0.99	0.01
Kokolik	2.3	1.9	2.6	0.008	−0.003	0.020	91	82	91	−9.4	0.97	0.01
Koyukuk-1	8.1	5.4	18.2	0.000	−0.008	0.009	50	32	61	−3.1	0.52	0.01
Koyukuk-2	12.4	6.1	22.5	0.007	−0.003	0.017	43	31	58	−3.2	0.52	0.01
Koyukuk-3	9.7	5.0	21.9	0.004	−0.006	0.015	50	39	62	−3.2	0.52	0.01
Koyukuk-4	7.4	4.4	21.9	0.004	−0.004	0.015	51	39	62	−3.4	0.53	0.01
Kuparuk	1.5	1.3	1.7	0.015	0.009	0.021	100	92	100	−10.8	0.92	0.01
Kuskokwim	2.8	2.0	19.8	0.011	0.000	0.023	20	9	51	−0.7	0.51	0.01
Mackenzie	19.9	7.2	28.2	0.012	0.001	0.026	-	-	-	−8.3	0.75	0.01
Nushagak	2.5	1.8	22.4	0.011	−0.001	0.025	0	0	7	1.6	0.50	0.01
Porcupine	17.6	4.4	27.7	−0.018	−0.038	−0.002	38	23	50	−4.4	0.55	0.01
Portage	2.5	2.1	19.8	0.013	0.000	0.027	0	0	7	1.6	0.50	0.01
Slave	32.4	14.8	44.9	0.000	−0.016	0.015	-	-	-	−2.2	0.27	0.01
Squirrel	4.8	3.8	6.5	0.022	0.012	0.032	73	55	89	−6.2	0.67	0.01
Tanana	14.8	9.1	24.1	−0.025	−0.065	0.004	50	38	62	−2.1	0.39	0.01
Yukon-Beaver	17.4	11.3	24.5	−0.002	−0.020	0.016	49	32	62	−4.0	0.47	0.01
Yukon-HW1	2.3	1.9	2.8	0.003	−0.005	0.011	82	73	90	−10.8	0.60	0.01
Yukon-HW2	2.8	1.9	3.4	−0.003	−0.013	0.005	73	54	82	−11.4	0.57	0.01

The columns labeled [50th], [25th], and [75th] list the 50th, 25th, and 75th percentiles, respectively, of the observed values for the floodplain surrounding each river reach. The temporal trend in the mean annual temperature (MAT) is calculated using ERA reanalysis[69].

https://doi.org/10.1038/s41558-025-02512-w

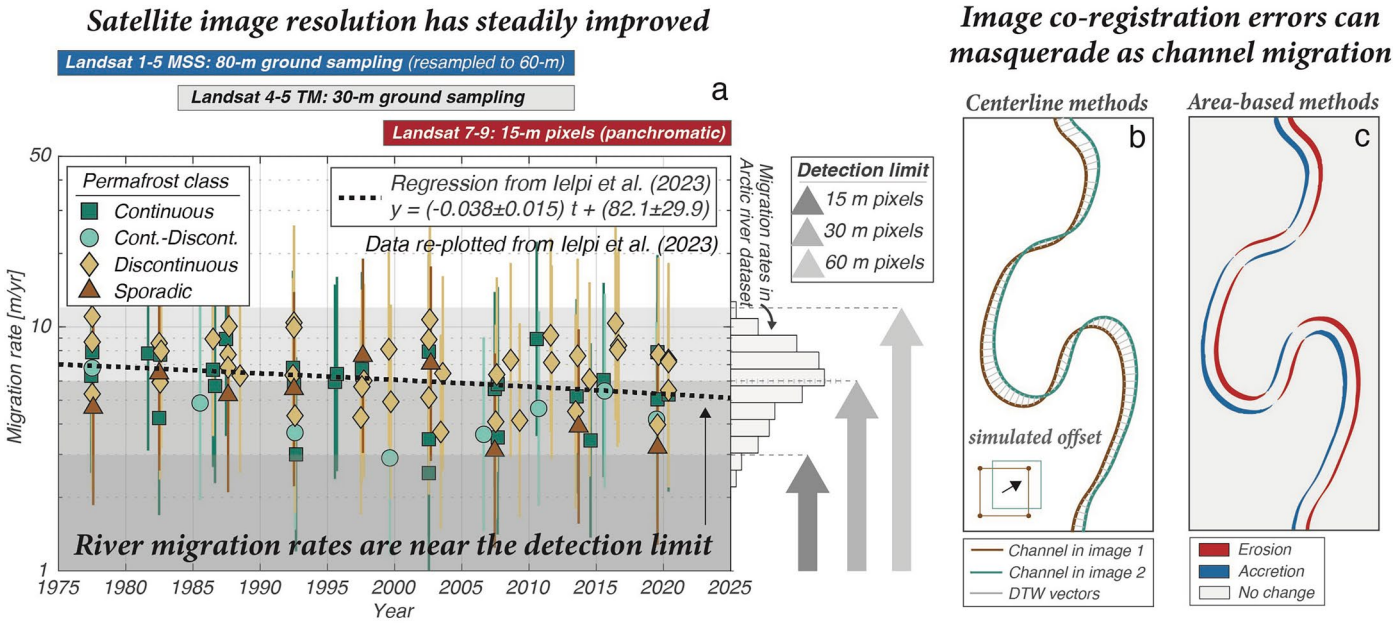

Extended Data Fig. 1 | Potential pitfalls of inferring changes to river migration rates from optical satellite timeseries. (**a**) There has been a secular change in the spatial resolution of optical satellite imagery from 1972 to present. Landsat 1-5 Multispectral Scanner (MSS) satellite images have 80 m ground sampling distance (often resampled to 60 m pixels), Landsat 4-5 Thematic Mapper (TM) images have 30 m resolution, and Landsat 7-9 images have a panchromatic band at 15-m resolution[14]. This monotonic change in image resolution coincides with a previously-inferred slowdown in Arctic river migration rates (measured at 5-year intervals by ref. 13). See ref. 13 for details. The histogram on the right side of (**a**) denotes the distribution of migration rates reported by ref. 13. Note that the reported[13] average migration rate of ~ 6.3 m yr^{-1} is approximately equal to the detection threshold for measuring one 30-m pixel of river migration within each studied 5-year interval (6.0 m yr^{-1}). In other words, the typical rates of river migration hover around the detection limit. (**b**-**c**) Image co-registration errors (such as the simple translation shown in **b**-**c**) can resemble channel migration and will erroneously be measured as such using the common centerline[13,38,39] and/or area-based[40,57] techniques.

https://doi.org/10.1038/s41558-025-02512-w

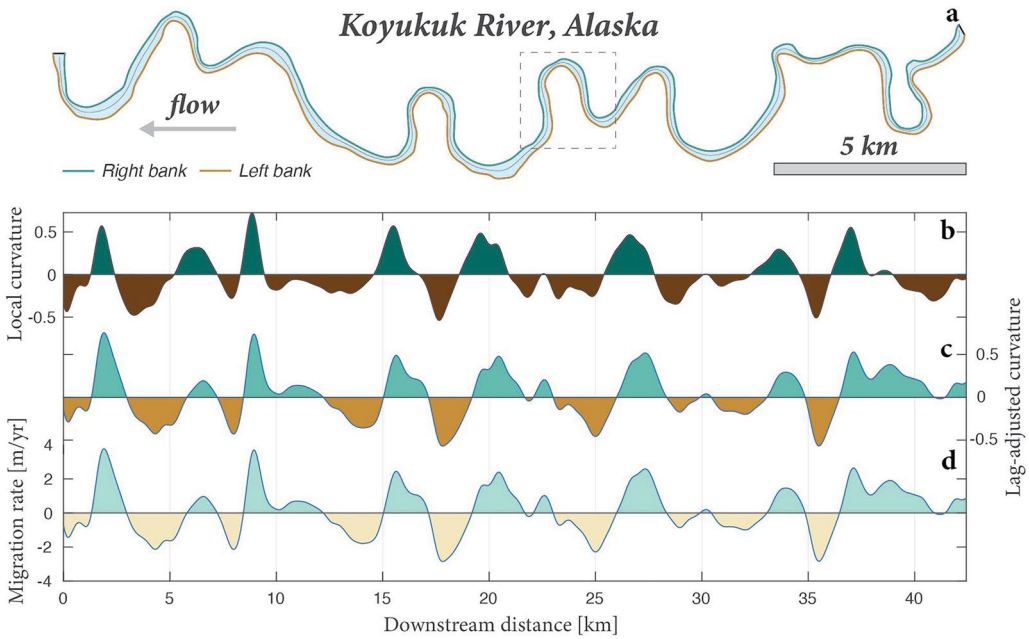

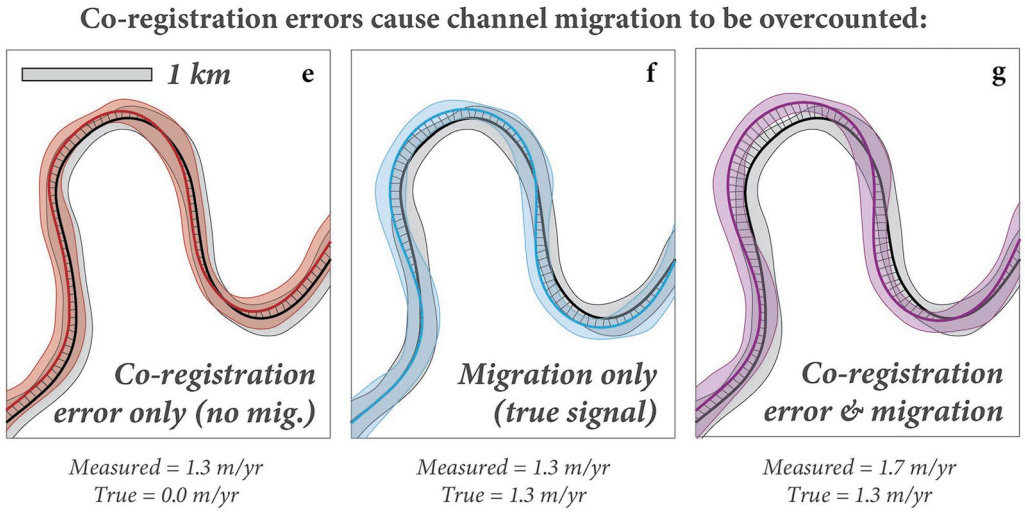

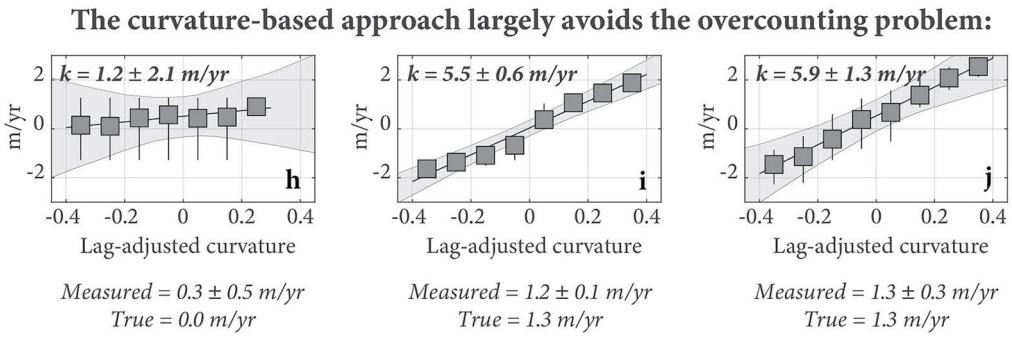

Extended Data Fig. 2 | An illustration of how our curvature-based approach avoids overcounting the apparent channel migration from image co-registration errors. (**a**) An example segment of the Koyukuk River (65.459°, −157.348°). (**b**-**d**) Streamwise profiles of (**b**) local normalized channel curvature, (**c**) lag-adjusted dimensionless curvature[38], and (**d**) simulated channel migration rate (which we define as a linear function of the lag-adjusted dimensionless curvature, as observed by ref. 11). (**e**-**f**) Zoom-in illustrations showing the altered channel boundaries as a result of: (**e**) lateral co-registration errors, (**f**) channel migration, and (**g**) both lateral co-registration errors and migration. Directly measuring channel displacement—for example, using the dynamic time warping (DTW) vectors plotted in black in (**e**-**f**)—results in an overestimate of channel migration because the co-registration errors are incorrectly counted as migration. (**h**-**j**) The curvature-based approach (see Methods) avoids the overcounting problem and leads to migration rate estimates that are within error of the true rates for all scenarios in (**e**-**f**). The error bars in (**h**-**j**) depict the 25-75th percentiles of the measured migration rates (*y*-axis) for each of the binned curvature values (*x*-axis). The error envelope depicts the ±1σ uncertainty of the linear fit through the binned data.

https://doi.org/10.1038/s41558-025-02512-w

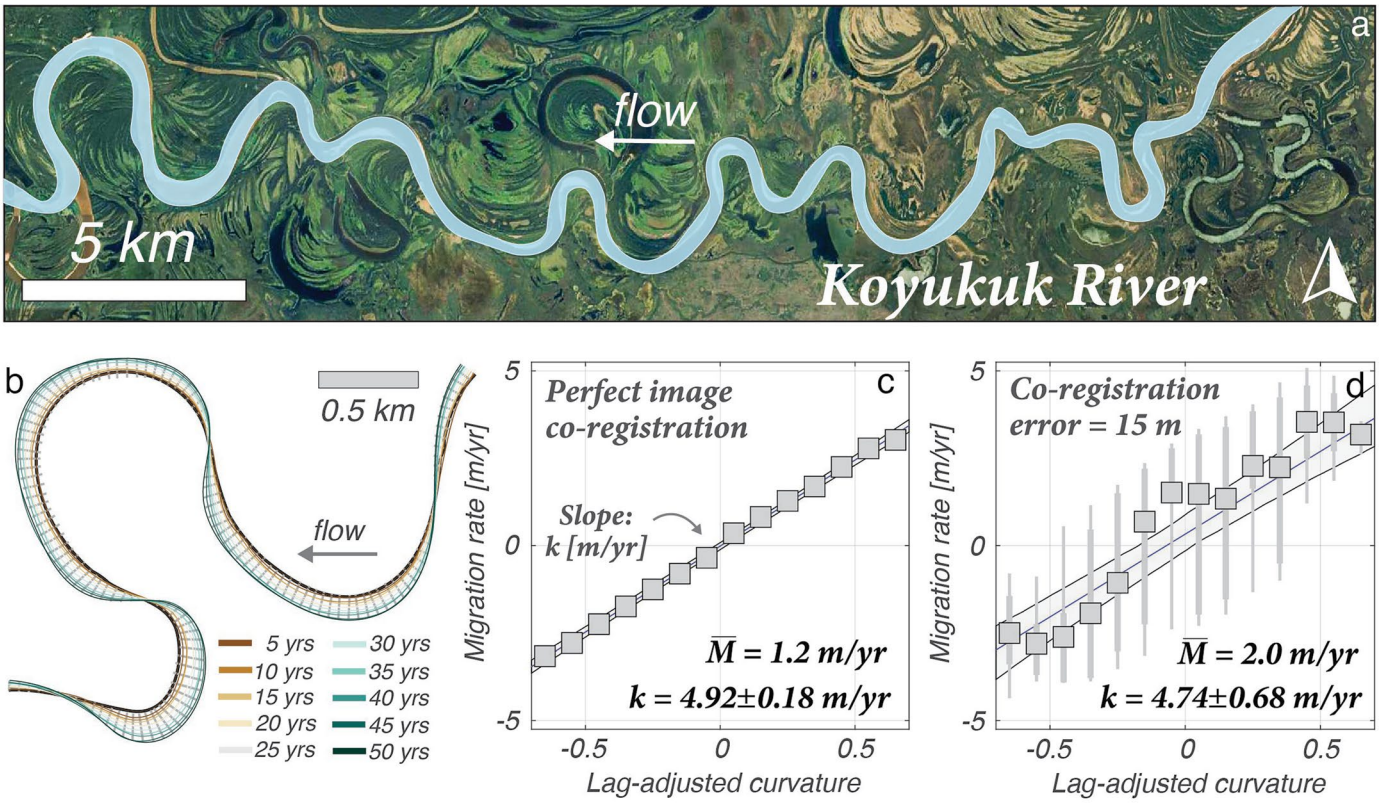

Extended Data Fig. 3 | A synthetic experiment to test for bias in the extraction of migration rates from historical Landsat timeseries. (**a**) An example reach of the Koyukuk River (Alaska) showing a sinuous planform of ~ 20 meander bends. Imagery: Google satellite basemap (image data from Maxar Technologies). (**b**) We simulate the meander evolution of the reach in (**a**) using the convolutional model of ref. 58 (see Methods). In the simulation in (**b**), we use an erodibility coefficient of $k = 5$ m yr^{-1}, which makes the spatially-averaged migration rate $M = 1.2$ m yr^{-1}. (**c**) Assuming perfect image co-registration, we can correctly recover the erodibility coefficient of $k = 5$ m yr^{-1} ($k = 4.92 \pm 0.18$ m yr^{-1}) from the simulated data in (**b**). (**d**) If there are co-registration errors between successive pairs of channel centerlines (in this case, produced using a simple translational shift of 15 m in a random direction), then the raw estimate of M is biased high ($M = 2.0$ m yr^{-1}) due to the fact that image co-registration errors are mistaken for channel migration (Extended Data Fig. 1b-c). However, using the curvature-based approach, we recover an estimate of the erodibility coefficient that has a larger uncertainty but still is within error of the true value ($k = 4.74 \pm 0.68$ m yr^{-1}). In other words, co-registration errors cause the estimate of k to be noisy, but not systematically biased. (**e**-**f**) Using the meander model[58] in (**b**), we simulate channel migration across the Landsat observational record under the null hypothesis of constant migration rate. Then, we sample the simulated dataset with co-registration errors informed by the Landsat history shown in Extended Data Fig. 1a. We assume that the co-registration errors are equal to one-half the pixel size. (**e**) The declining co-registration errors with time cause the migration rates quantified directly using dynamic time warping[13,38] to appear to be decreasing at a rate of − 19 ± 4.6% per decade, even though the true migration rate is constant with time. (**f**) The declining co-registration errors with time do not cause a large trend in the estimate of the erodibility coefficient. The magnitude of the trend shown in (**f**) is approximately 7 × smaller than that shown in (**e**). The error bars in (**d**) depict the 10-90th percentiles (thin) and 25-75th percentiles (thick) of the binned data. The error bars in (**e**-**f**) depict the 5-95th percentiles of the simulated migration rates.